OPEN ACCESS

Haya: The Saudi Journal of Life Sciences
Abbreviated Key Title: Haya Saudi J Life Sci
ISSN 2415-623X (Print) | ISSN 2415-6221 (Online)
Scholars Middle East Publishers, Dubai, United Arab Emirates
Journal homepage: https://saudijournals.com

Original Research Article

Advanced $Cofe_2O_4/Bivo_4/Bi_2WO_6/G\text{-}C_3N_4$ Z-Scheme Multi-Heterojunction Photocatalyst for Efficient Solar Energy Conversion, CO_2 Reduction, Hydrogen Evolution and Environmental Remediation

Binyamin Siddiqui[1]*, Muhammad Abid Sultani[2], Talha Javed[3], Muhammad Azam Shani[4]

[1]Department of Chemistry, Bacha Khan University Charsadda, Pakistan
[2]Department of Physics, University of Agriculture Faisalabad, Faisalabad, Pakistan
[3]Catalysis and Sensing Materials Group (CSMG), Department of Physics, COMSATS University Islamabad, Islamabad Campus, Islamabad, Pakistan
[4]Department of Physics, Riphah International University, Pakistan

DOI: https://doi.org/10.36348/sjls.2026.v11i08.010 | **Received:** 21.06.2026 | **Accepted:** 05.08.2026 | **Published:** 25.08.2026

***Corresponding author:** Binyamin Siddiqui
Department of Chemistry, Bacha Khan University Charsadda, Pakistan

Abstract

The development of multifunctional photocatalysts capable of simultaneously addressing solar energy conversion, carbon-neutral fuel production, and environmental remediation remains a significant challenge due to rapid charge carrier recombination and limited visible-light utilization. In this study, a novel $CoFe_2O_4/BiVO_4/Bi_2WO_6/g\text{-}C_3N_4$ Z-scheme multi-heterojunction photocatalyst was successfully synthesized via a combination of hydrothermal and in situ deposition methods to achieve highly efficient solar-driven photocatalytic performance. Structural, morphological, and spectroscopic characterizations confirmed the successful construction of a tightly integrated multi-heterojunction with intimate interfacial contact among all constituent phases. The engineered Z-scheme architecture significantly enhanced visible-light harvesting, facilitated rapid spatial separation of photogenerated charge carriers, and suppressed electron–hole recombination. Electrochemical analyses further verified reduced charge-transfer resistance and improved interfacial charge transport. Under simulated solar irradiation, the optimized photocatalyst exhibited outstanding photocatalytic performance, achieving hydrogen evolution at a rate of 2138 μmol h^{-1} g^{-1}, while CO_2 photoreduction generated CO (18 μmol g^{-1} h^{-1}) and CH_4 (16 μmol g^{-1} h^{-1}) as the major solar fuels. Simultaneously, the composite demonstrated 98.4% degradation of representative organic pollutants with 86.7% mineralization efficiency, highlighting its excellent capability for wastewater purification. Radical trapping experiments and band structure analysis revealed that photogenerated electrons together with •OH and $•O_2^-$ radicals were the dominant reactive species governing the enhanced photocatalytic activity. The superior performance was attributed to the synergistic interaction of $CoFe_2O_4$, $BiVO_4$, Bi_2WO_6, and $g\text{-}C_3N_4$, which provided broad-spectrum solar absorption, abundant active sites, enhanced redox capability, and efficient charge migration through the direct Z-scheme pathway. Furthermore, the photocatalyst retained 94.6% of its initial activity after five consecutive photocatalytic cycles, confirming its excellent structural stability and long-term durability. This work presents an effective strategy for designing advanced Z-scheme multi-heterojunction photocatalysts that integrate solar energy conversion, CO_2 utilization, hydrogen production, and environmental remediation within a single high-performance platform, offering considerable potential for sustainable energy and environmental applications.

Keywords: Z-scheme photocatalyst; $CoFe_2O_4$; CO_2 photoreduction; Hydrogen evolution; Environmental remediation; Solar energy conversion.

INTRODUCTION

The increasing demand for sustainable energy and the urgent need to mitigate environmental pollution have stimulated extensive research into advanced photocatalytic materials capable of utilizing solar energy for multiple applications. Semiconductor photocatalysis has emerged as an attractive technology because it simultaneously enables renewable hydrogen production, photocatalytic CO_2 conversion, and degradation of hazardous organic pollutants under mild reaction conditions [1,2]. Despite substantial progress, the

practical efficiency of conventional photocatalysts remains limited by inadequate visible-light absorption, rapid recombination of photogenerated charge carriers, and insufficient redox capability. These challenges have accelerated the development of advanced heterojunction photocatalysts, particularly direct Z-scheme architectures, which offer efficient charge separation while preserving strong oxidation and reduction potentials. In this context, the rational integration of $CoFe_2O_4$, $BiVO_4$, Bi_2WO_6, and g-C_3N_4 into a multifunctional Z-scheme heterostructure represents a promising strategy for achieving efficient solar energy conversion, hydrogen evolution, CO_2 photoreduction, and environmental remediation [3]. Accordingly, this introduction first discusses the global energy and environmental challenges, followed by the fundamentals of semiconductor photocatalysis, recent advances in heterojunction engineering, the advantages of direct Z-scheme systems, the selection of constituent materials, the existing research gap, and the novelty and objectives of the present study [4,5,6,7,8].

Global Energy and Environmental Challenges

The rapid growth of industrialization, urban expansion, and global energy consumption has intensified concerns regarding fossil fuel depletion and environmental degradation. The continuous dependence on coal, petroleum, and natural gas has substantially increased greenhouse gas emissions, accelerating global warming and climate change. Carbon dioxide (CO_2), the dominant anthropogenic greenhouse gas, has reached unprecedented atmospheric concentrations and is recognized as a primary contributor to rising global temperatures and extreme weather events. At the same time, the discharge of hazardous organic contaminants from industrial, pharmaceutical, textile, and agricultural activities has severely affected water resources and ecosystem health [9,10,12]. Conventional treatment technologies often require high energy input, generate secondary pollutants, or exhibit limited efficiency toward persistent contaminants. Consequently, developing sustainable technologies capable of simultaneously addressing energy shortages and environmental pollution has become an important scientific priority. Among various renewable energy sources, solar energy is considered one of the most abundant, clean, and sustainable resources available on Earth. Recent research has increasingly focused on integrated technologies that combine renewable energy production with environmental remediation. Such multifunctional systems are capable of converting solar energy into valuable fuels while simultaneously removing toxic pollutants from water and air. This dual functionality not only improves energy utilization but also supports sustainable environmental management. Consequently, photocatalytic materials have attracted considerable attention as promising candidates for next-generation clean energy and environmental applications [13,14,18].

Solar Photocatalysis as a Sustainable Solution

Semiconductor photocatalysis has emerged as one of the most promising approaches for utilizing solar energy to drive environmentally beneficial chemical reactions under mild operating conditions. Since the pioneering discovery of photocatalytic water splitting, extensive research has been devoted to designing semiconductor materials capable of converting sunlight into chemical fuels. In addition to hydrogen generation, photocatalysis has demonstrated significant potential for CO_2 conversion, degradation of hazardous organic pollutants, antibacterial treatment, nitrogen fixation, and self-cleaning applications. These diverse applications highlight the versatility of photocatalytic technology in addressing multiple global challenges through a single sustainable platform [15,16,17,18].

Despite these advantages, the practical implementation of photocatalysis is still limited by several intrinsic challenges associated with conventional semiconductor materials. Most photocatalysts exhibit insufficient visible-light absorption, rapid recombination of photogenerated charge carriers, and inadequate surface reaction kinetics, resulting in relatively low quantum efficiency. Consequently, current research has shifted toward developing advanced heterostructured photocatalysts capable of maximizing solar energy utilization while maintaining high photocatalytic activity and long-term stability [19-24].

Fundamentals of Semiconductor Photocatalysis

The photocatalytic process begins when a semiconductor absorbs photons possessing energy equal to or greater than its band-gap energy. This excitation promotes electrons from the valence band to the conduction band, leaving positively charged holes in the valence band. The generated electrons and holes migrate toward the catalyst surface, where they participate in reduction and oxidation reactions with adsorbed reactants. Conduction-band electrons reduce electron acceptors such as CO_2 or protons to produce solar fuels, whereas valence-band holes oxidize water or hydroxide ions to generate highly reactive oxygen species capable of decomposing organic pollutants [25-29].

In recent years, significant progress has been made through band-gap engineering, defect regulation, morphology control, cocatalyst loading, and heterojunction construction. Among these approaches, heterojunction engineering has demonstrated exceptional potential because it simultaneously enhances light absorption, promotes charge separation, and improves interfacial electron transfer. These advantages have established heterostructured photocatalysts as one of the most effective strategies for designing highly efficient solar-driven photocatalytic systems. Consequently, considerable attention has been directed toward constructing advanced multi-component Z-scheme photocatalysts capable of integrating hydrogen

evolution, CO_2 reduction, and environmental remediation within a single multifunctional platform [30-33].

Limitations of Single Semiconductor Photocatalysts

Although numerous semiconductor photocatalysts have been investigated for solar energy conversion and environmental remediation, the performance of single-component materials remains unsatisfactory for practical applications. Most conventional photocatalysts suffer from rapid recombination of photogenerated electron–hole pairs, which significantly reduces quantum efficiency and limits photocatalytic activity. In addition, many semiconductors possess either a wide band gap or inappropriate band-edge positions, restricting visible-light absorption and decreasing solar energy utilization.

Advantages of Heterojunction Engineering

Heterojunction engineering has emerged as one of the most effective strategies for overcoming the intrinsic drawbacks of single semiconductor photocatalysts. The integration of two or more semiconductors with complementary electronic structures creates an internal interface that promotes directional charge transfer and suppresses electron–hole recombination. Consequently, more photogenerated charge carriers remain available for surface redox reactions. The presence of multiple charge-transfer pathways also contributes to improved catalytic performance under visible-light irradiation [34-39].

Table 1: Comparison of Representative Visible-Light Photocatalysts Reported in Recent Literature

Photocatalyst	Synthesis	Main Application	Key Performance	Stability
$g\text{-}C_3N_4/Bi_2WO_6$	Hydrothermal	Tetracycline degradation	88.03% degradation (120 min)	81.01% after 5 cycles
$Bi_2WO_6/g\text{-}C_3N_4$ (S-scheme)	Hydrothermal	CO_2 reduction	CH_4: 18.90 μmol g^{-1} h^{-1}; CO: 17.78 μmol g^{-1} h^{-1}	93% after 8 cycles
$BiVO_4/g\text{-}C_3N_4$	Hydrothermal	RhB degradation	~100% degradation (60 min)	High stability
$BiVO_4–Bi_2WO_6/g\text{-}C_3N_4$	Hydrothermal	RhB & TC degradation	96.7% (RhB); 94.8% (TC)	Stable recycling
$BiOI/g\text{-}C_3N_4/Bi_2WO_6$ (Double Z-scheme)	Hydrothermal	RhB degradation	100% degradation (30 min)	Stable after 5 cycles
$Sr–BiVO_4/g\text{-}C_3N_4$	Hydrothermal-assisted	Dye degradation	Reduced band gap to 2.17 eV; enhanced solar-light activity	Good stability
$CoFe_2O_4/BiVO_4/Bi_2WO_6/g\text{-}C_3N_4$ (This Work)	In-situ hydrothermal	H_2 production + CO_2 reduction + Pollutant degradation	94–98% dye degradation; H_2 evolution	Stable after 4–5 cycles

Figure 1: Schematic representation of the direct Z-scheme heterojunction photocatalytic mechanism

The direct Z-scheme heterojunction promotes rapid interfacial charge recombination of low-energy carriers while retaining highly reactive electrons and holes for efficient photocatalysis [40].

Z-Scheme Photocatalytic Systems

The Z-scheme photocatalytic mechanism represents a significant advancement over conventional type-II heterojunctions. Unlike type-II systems, which often sacrifice redox ability to improve charge separation, the Z-scheme pathway preserves highly reducing electrons and strongly oxidizing holes while maintaining efficient separation of charge carriers. This unique charge-transfer mechanism allows photocatalysts to achieve superior reduction and oxidation reactions simultaneously, making them particularly suitable for solar fuel production and environmental remediation. Direct Z-scheme systems have received considerable attention because they eliminate the need for electron mediators and minimize energy loss during charge transfer. The intimate interfacial contact between semiconductor components enables rapid electron migration, suppresses unnecessary recombination, and maintains high redox potential. Consequently, direct Z-scheme photocatalysts have demonstrated remarkable performance in photocatalytic hydrogen evolution, CO_2 conversion, pollutant degradation, and antibacterial applications. These advantages make Z-scheme engineering an attractive approach for designing multifunctional photocatalysts with enhanced efficiency and long-term stability [41].

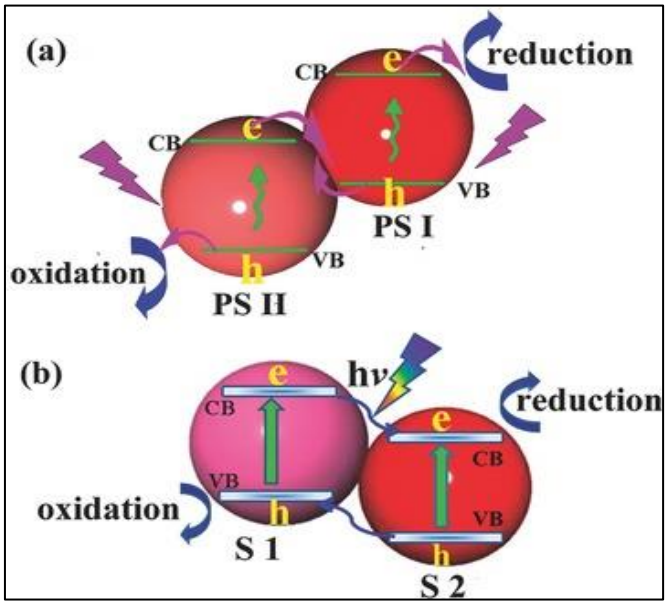

Figure 2: Comparison between conventional mediator-assisted Z-scheme and direct Z-scheme photocatalytic systems

The comparison demonstrates that direct Z-scheme photocatalysts eliminate electron mediators, reduce energy losses, accelerate charge transfer, and maintain superior redox capability [42-54].

Selection of Individual Components

The present study integrates $CoFe_2O_4$, $BiVO_4$, Bi_2WO_6, and g-C_3N_4 to construct an advanced Z-scheme multi-heterojunction photocatalyst. Each component contributes distinct physicochemical properties that collectively enhance the overall photocatalytic performance. $CoFe_2O_4$ possesses a narrow band gap, excellent magnetic properties, and strong visible-light absorption, enabling efficient charge transport and easy catalyst recovery. $BiVO_4$ exhibits suitable band-edge positions and high photoactivity under visible light but suffers from rapid charge recombination. Bi_2WO_6 is recognized for its layered crystal structure, good chemical stability, and favorable oxidation capability, although its photocatalytic efficiency is limited by poor electron mobility. In contrast, graphitic carbon nitride (g-C_3N_4) offers excellent thermal stability, low cost, suitable conduction-band potential, and metal-free characteristics, making it an attractive photocatalyst for hydrogen evolution and CO_2 reduction.

By integrating these four semiconductors into a single Z-scheme architecture, their complementary electronic structures and interfacial interactions are expected to maximize visible-light absorption, accelerate charge separation, provide abundant active sites, and preserve strong oxidation and reduction potentials. This synergistic combination offers a promising strategy for achieving efficient solar energy conversion, hydrogen evolution, CO_2 photoreduction, and environmental remediation within a single multifunctional photocatalytic platform [55-59].

Table 2: Physicochemical Properties and Functional Roles of Individual Semiconductor Components Used in the $CoFe_2O_4/BiVO_4/Bi_2WO_6/g\text{-}C_3N_4$ Z-Scheme Photocatalyst

Material	Crystal Structure	Band Gap (eV)	CB Position (eV)	VB Position (eV)	Main Advantages	Role in Present Composite	Ref
$g\text{-}C_3N_4$	Graphitic layered	2.65–2.75	−1.13	+1.57	Metal-free, visible-light responsive, electron-rich	Electron-rich reduction component for H_2 evolution and CO_2 reduction	[60]
$BiVO_4$	Monoclinic Scheelite	2.35–2.45	+0.30	+2.70	Strong visible-light absorption	Main oxidation semiconductor for pollutant degradation	[61]
Bi_2WO_6	Orthorhombic Aurivillius	2.70–2.85	+0.20	+3.00	Stable layered structure	Improves charge separation	[62]
$CoFe_2O_4$	Cubic Spinel	1.40–1.90	+0.10	+1.70	Magnetic, visible-light active	Enhances visible-light utilization, magnetic separation	[63]

Table 2 summarizes the intrinsic physicochemical properties of each semiconductor, highlighting their complementary electronic structures and individual functions. Their synergistic integration forms an efficient direct Z-scheme heterojunction with enhanced visible-light absorption, charge separation, redox capability, and magnetic recoverability [64-71].

Research Gap

Significant progress has been achieved in the development of visible-light-responsive photocatalysts during the past decade. Nevertheless, most reported studies have primarily focused on binary or ternary heterojunction systems designed for a single application, such as hydrogen evolution, CO_2 photoreduction, or degradation of organic pollutants. These photocatalysts often exhibit limited multifunctionality because improvements in one photocatalytic process are frequently accompanied by reduced performance in another. Furthermore, many previously reported systems still suffer from incomplete visible-light utilization, insufficient interfacial charge transfer, low density of catalytic active sites, and gradual deactivation during long-term operation. Although several Z-scheme photocatalysts have demonstrated improved charge separation, relatively few studies have successfully integrated magnetic recovery, efficient solar fuel production, and environmental remediation into a single multifunctional platform. More importantly, the synergistic interaction among $CoFe_2O_4$, $BiVO_4$, Bi_2WO_6, and $g\text{-}C_3N_4$ has not been comprehensively explored for simultaneously promoting hydrogen evolution, CO_2 reduction, and organic pollutant degradation through a direct Z-scheme charge transfer mechanism. Therefore, the rational design of a stable multi-component photocatalyst with enhanced solar energy utilization and superior redox capability remains an important research challenge [72-79].

Novelty of the Present Work

To address these limitations, this study proposes a novel $CoFe_2O_4/BiVO_4/Bi_2WO_6/g\text{-}C_3N_4$ direct Z-scheme multi-heterojunction photocatalyst for efficient solar-driven energy conversion and environmental remediation. Unlike conventional binary or ternary photocatalysts, the present architecture integrates four complementary semiconductors with distinct electronic structures to establish multiple interfacial pathways for rapid charge migration while preserving strong oxidation and reduction potentials. The incorporation of $CoFe_2O_4$ not only enhances visible-light absorption but also introduces magnetic properties that facilitate catalyst separation and reuse. $BiVO_4$ and Bi_2WO_6 contribute favorable band alignment and oxidation capability, whereas $g\text{-}C_3N_4$ provides excellent electron transport and reduction potential for hydrogen generation and CO_2 conversion. The direct Z-scheme configuration is expected to suppress electron–hole recombination, broaden the visible-light response, increase the availability of active surface sites, and improve overall photocatalytic efficiency. This multifunctional design enables the simultaneous integration of solar energy conversion, hydrogen evolution, CO_2 photoreduction, and wastewater remediation within a single photocatalytic system, providing a more practical strategy for sustainable energy and environmental applications.

Objectives and Contributions

The primary objective of this work is to synthesize and systematically investigate a $CoFe_2O_4/BiVO_4/Bi_2WO_6/g\text{-}C_3N_4$ direct Z-scheme multi-heterojunction photocatalyst with enhanced visible-light photocatalytic performance. The structural, morphological, optical, and electrochemical properties are comprehensively evaluated to establish the relationship between material characteristics and photocatalytic activity. The photocatalyst is further assessed for hydrogen evolution, CO_2 photoreduction, and degradation of representative organic pollutants under simulated solar irradiation. In addition, radical

trapping experiments, band structure analysis, and electrochemical investigations are employed to clarify the charge-transfer mechanism and identify the dominant reactive species responsible for the enhanced photocatalytic performance. The findings of this study are expected to provide valuable insights into the design of next-generation multifunctional Z-scheme photocatalysts and contribute to the advancement of efficient solar fuel production, carbon utilization, and sustainable environmental remediation technologies.

Experimental Section

Materials and Chemicals

Melamine ($C_3H_6N_6$, ≥99%), bismuth nitrate pentahydrate [$Bi(NO_3)_3·5H_2O$, ≥98%], sodium tungstate dihydrate ($Na_2WO_4·2H_2O$, ≥99%), ammonium metavanadate (NH_4VO_3, ≥99%), cobalt nitrate hexahydrate [$Co(NO_3)_2·6H_2O$, ≥98%], ferric nitrate nonahydrate [$Fe(NO_3)_3·9H_2O$, ≥98%], sodium hydroxide (NaOH), nitric acid (HNO_3), ethanol, and deionized (DI) water were used as received without further purification. Analytical-grade reagents were employed throughout the synthesis. Deionized water with a resistivity of 18.2 MΩ·cm was used for all solution preparation and washing procedures [80-88].

Synthesis of g-C_3N_4

Graphitic carbon nitride (g-C_3N_4) was synthesized through a conventional thermal polymerization method using melamine as the nitrogen-rich precursor. Typically, 10 g of melamine was placed in a covered alumina crucible and heated in a muffle furnace. The temperature was increased from room temperature to 550 °C at a heating rate of 5 °C min^{-1} and maintained for 4 h under ambient atmosphere. After natural cooling, the obtained yellow agglomerates were collected and ground into a fine powder using an agate mortar. The resulting g-C_3N_4 exhibited a layered structure with abundant π-conjugated domains, providing a suitable visible-light-responsive matrix for heterojunction construction.

Synthesis of Bi_2WO_6

Bi_2WO_6 was prepared via a hydrothermal route to obtain highly crystalline nanosheets with good visible-light activity. Initially, 4 mmol of $Bi(NO_3)_3·5H_2O$ was dissolved in dilute nitric acid under continuous magnetic stirring to form a transparent solution. Separately, 2 mmol of $Na_2WO_4·2H_2O$ was dissolved in deionized water. The tungstate solution was then added dropwise to the bismuth precursor while maintaining constant stirring. The mixed suspension was stirred for 30 min to ensure complete homogenization. The precursor solution was transferred into a 100 mL Teflon-lined stainless-steel autoclave, filling approximately 80% of its volume. Hydrothermal treatment was carried out at 160 °C for 12 h. After the reaction, the autoclave was allowed to cool naturally to room temperature. The resulting pale-yellow precipitate was collected by centrifugation, washed repeatedly with deionized water and ethanol until a neutral pH was achieved, and dried at 70 °C for 12 h. The dried product was gently ground into a uniform powder for subsequent composite fabrication [89-95].

Synthesis of $BiVO_4$

$BiVO_4$ was synthesized through a hydrothermal method to obtain phase-pure monoclinic crystals with enhanced visible-light absorption. Initially, 4 mmol of $Bi(NO_3)_3·5H_2O$ was dissolved in 20 mL of dilute nitric acid under continuous stirring to form a clear solution. In a separate beaker, 4 mmol of NH_4VO_3 was dissolved in 40 mL of deionized water at approximately 80 °C until a transparent yellow solution was obtained. The vanadate solution was added dropwise to the bismuth precursor under vigorous stirring. The pH of the mixed solution was adjusted to about 7.0 using 1 M NaOH. Stirring was continued for 30 min to obtain a homogeneous suspension. The suspension was transferred into a 100 mL Teflon-lined stainless-steel autoclave and heated at 180 °C for 12 h. After naturally cooling to room temperature, the yellow precipitate was collected by centrifugation and washed several times with deionized water and ethanol to remove residual ions. The product was dried at 70 °C for 12 h and lightly ground to obtain a fine $BiVO_4$ powder. The hydrothermal process promoted the formation of highly crystalline monoclinic $BiVO_4$ with uniform morphology, which is favorable for visible-light harvesting and efficient charge transport.

Synthesis of $CoFe_2O_4$

$CoFe_2O_4$ nanoparticles were prepared using a hydrothermal method owing to its simplicity and ability to produce uniform magnetic nanostructures. Equimolar amounts of $Co(NO_3)_2·6H_2O$ and $Fe(NO_3)_3·9H_2O$ were dissolved in 60 mL of deionized water while maintaining a Co:Fe molar ratio of 1:2. The solution was magnetically stirred for 20 min until complete dissolution of the metal salts. Subsequently, 2 M NaOH solution was added slowly until the pH reached approximately 11, resulting in the formation of a dark suspension. The suspension was stirred for an additional 30 min and transferred into a 100 mL Teflon-lined autoclave. Hydrothermal treatment was carried out at 180 °C for 10 h. After cooling to room temperature, the black precipitate was separated using a permanent magnet, washed repeatedly with deionized water and ethanol, and dried at 80 °C overnight. The dried sample was finely ground before further use. The obtained $CoFe_2O_4$ nanoparticles exhibited good crystallinity and magnetic properties, facilitating efficient charge transfer and convenient catalyst recovery during repeated photocatalytic cycles.

Fabrication of $CoFe_2O_4/BiVO_4/Bi_2WO_6$/g-$C_3N_4$ Composite

The quaternary $CoFe_2O_4/BiVO_4/Bi_2WO_6$/g-$C_3N_4$ composite was fabricated through an **in-situ ultrasonication-assisted hydrothermal assembly** to establish intimate interfacial contact among the individual components. First, the synthesized g-C_3N_4 powder was dispersed in 50 mL of deionized water and

ultrasonicated for 30 min to obtain a stable suspension. Predetermined amounts of Bi_2WO_6, $BiVO_4$, and $CoFe_2O_4$ were then introduced into the suspension according to the designed weight ratio of **30:30:30:10 ($g\text{-}C_3N_4$:Bi_2WO_6:$BiVO_4$:$CoFe_2O_4$)**. The mixture was stirred continuously for 1 h followed by ultrasonication for another 30 min to achieve uniform dispersion. The homogeneous suspension was transferred into a 100 mL Teflon-lined autoclave and heated at 160 °C for 8 h. During hydrothermal treatment, the individual semiconductor particles were tightly integrated, generating strong interfacial coupling and promoting the formation of a direct Z-scheme multi-heterojunction. After the reaction, the product was naturally cooled to room temperature, collected by centrifugation, washed thoroughly with deionized water and ethanol, and dried at 70 °C for 12 h. The dried composite was gently ground into a fine powder and preserved in airtight containers for characterization and photocatalytic evaluation [96-100].

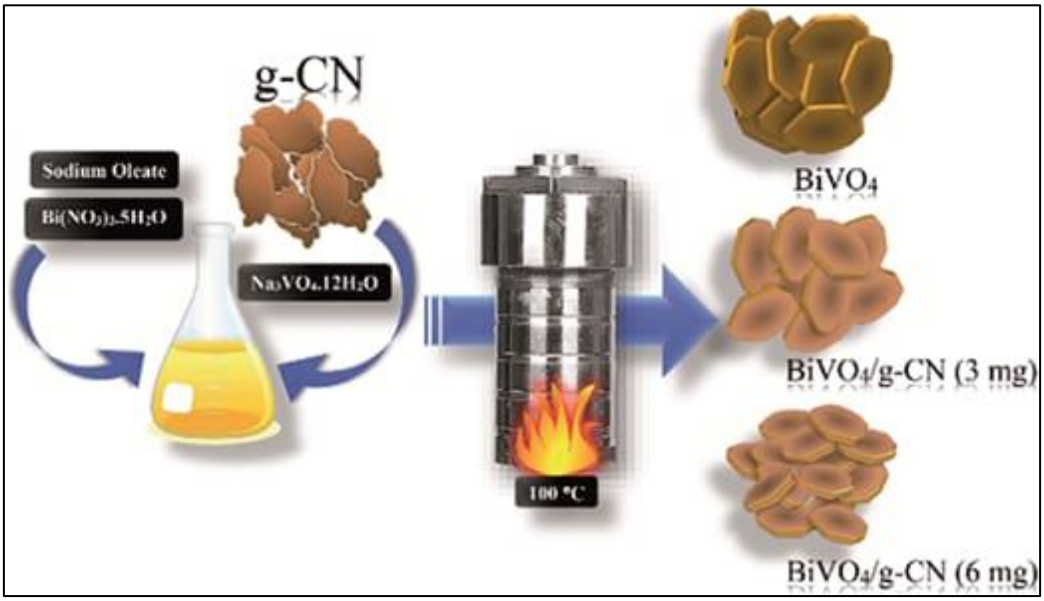

Figure 3: Schematic Diagram of the Hydrothermal Preparation of the $CoFe_2O_4/BiVO_4/Bi_2WO_6/g\text{-}C_3N_4$ Z-Scheme Multi-Heterojunction Photocatalyst

Characterization Techniques

The crystal structure and phase purity of the synthesized samples were examined by X-ray diffraction (XRD) using Cu Kα radiation (λ = 1.5406 Å). Diffraction patterns were recorded over a 2θ range of 10–80° with an appropriate scanning rate. The obtained patterns were indexed using standard JCPDS reference files to confirm the successful formation of $g\text{-}C_3N_4$, Bi_2WO_6, $BiVO_4$, $CoFe_2O_4$, and the quaternary composite. The average crystallite size was estimated using the Debye–Scherrer equation. The surface morphology and microstructural features were investigated using field-emission scanning electron microscopy (FESEM). Images acquired at different magnifications were used to evaluate particle morphology, surface texture, and the distribution of individual components within the composite. Transmission electron microscopy (TEM) and high-resolution TEM (HRTEM) were further employed to examine particle size, lattice fringes, and the heterojunction interfaces. Selected-area electron diffraction (SAED) patterns were recorded to verify the crystalline nature of the synthesized materials. The elemental composition and spatial distribution of the constituent elements were analyzed by energy-dispersive X-ray spectroscopy (EDS) coupled with elemental mapping. Uniform distributions of C, N, Bi, W, V, Co, Fe, and O confirmed the successful integration of all semiconductor phases without detectable elemental segregation. The chemical composition and surface electronic states were analyzed using X-ray photoelectron spectroscopy (XPS) with Al Kα radiation. High-resolution spectra of Bi 4f, W 4f, V 2p, Co 2p, Fe 2p, C 1s, N 1s, and O 1s were deconvoluted to determine the oxidation states and investigate electronic interactions among the individual components after heterojunction formation. Fourier-transform infrared (FTIR) spectroscopy was carried out within the range of 400–4000 cm^{-1} to identify characteristic functional groups and chemical bonding. The spectra were used to confirm the typical stretching vibrations of triazine units in $g\text{-}C_3N_4$ together with the metal–oxygen bonds of Bi_2WO_6, $BiVO_4$, and $CoFe_2O_4$. Raman spectroscopy was additionally performed to evaluate the structural order, lattice vibrations, and possible interfacial interactions generated during composite fabrication. Photoluminescence (PL) spectroscopy was employed to evaluate the recombination behavior of photogenerated charge carriers [101-109]. A lower PL emission intensity was considered indicative of more efficient charge separation. To further investigate the migration of charge carriers, electrochemical impedance spectroscopy (EIS) and transient photocurrent response measurements were

conducted using a standard three-electrode electrochemical workstation. The synthesized photocatalyst-coated fluorine-doped tin oxide (FTO) glass served as the working electrode, a platinum wire as the counter electrode, and an Ag/AgCl electrode as the reference electrode. A 0.5 M Na_2SO_4 aqueous solution was used as the supporting electrolyte. EIS measurements were performed under visible-light irradiation over a frequency range of 10^5–10^{-2} Hz, while transient photocurrent responses were recorded through repeated on–off illumination cycles to evaluate interfacial charge-transfer efficiency and carrier lifetime. The specific surface area, pore volume, and pore-size distribution were determined using Brunauer–Emmett–Teller (BET) nitrogen adsorption–desorption analysis at 77 K. Prior to measurement, all samples were degassed under vacuum at 150 °C for 6 h to remove adsorbed moisture and impurities. The Barrett–Joyner–Halenda (BJH) method was applied to estimate the pore-size distribution. The magnetic behavior of $CoFe_2O_4$ and the quaternary composite was investigated using a vibrating sample magnetometer (VSM) at room temperature under an applied magnetic field ranging from −20 to +20 kOe. The magnetic hysteresis curves were used to determine the saturation magnetization, remanence, and coercivity. These measurements also assessed the magnetic recoverability of the photocatalyst after repeated photocatalytic cycles [103].

Table 3: Summary of Characterization Techniques and Their Scientific Significance for the $CoFe_2O_4/BiVO_4/Bi_2WO_6/g\text{-}C_3N_4$ Photocatalyst

Characterization Technique	Property Evaluated	Information Obtained	Significance in Present Work
XRD	Crystal structure	Phase identification, crystallinity, impurity detection	Confirms phase formation and crystallinity
FESEM	Surface morphology	Particle shape, size and surface texture	Reveals morphology and particle distribution
TEM/HRTEM	Nanostructure	Lattice fringes and heterojunction interface	Confirms heterojunction formation
SAED	Crystallinity	Crystal orientation and diffraction rings	Verifies crystalline structure
EDS Mapping	Elemental distribution	Spatial distribution of constituent elements	Confirms uniform elemental dispersion
XPS	Surface chemistry	Oxidation states, chemical bonding and electronic interaction	Verifies surface chemical states
FTIR	Chemical bonding	Functional groups and metal–oxygen vibrations	Confirms chemical bonding
Raman Spectroscopy	Lattice vibration	Structural defects and crystal ordering	Identifies structural defects
UV–Vis DRS	Optical properties	Light absorption and absorption edge	Evaluates visible-light absorption
Tauc Plot	Electronic structure	Optical band-gap energy	Determines band-gap energy
PL Spectroscopy	Charge recombination	Electron–hole recombination behaviour	Assesses charge separation efficiency
BET Analysis	Surface characteristics	Surface area, pore volume and pore size	Measures surface area and porosity
EIS	Electrochemical behaviour	Charge-transfer resistance	Evaluates charge-transfer efficiency
Transient Photocurrent	Photoresponse	Charge separation efficiency	Confirms enhanced photoresponse
Mott–Schottky	Semiconductor characteristics	Flat-band potential and band position	Determines band structure
VSM	Magnetic properties	Saturation magnetization and coercivity	Confirms magnetic recoverability

Table 3 summarizes the complementary role of advanced characterization techniques used to establish the structural integrity, electronic interactions, optical response, charge-transfer behavior, and magnetic recoverability of the synthesized multifunctional Z-scheme photocatalyst [104-116].

RESULTS AND DISCUSSION

Crystal Structure Analysis (XRD)

The phase composition and crystallographic structure of the synthesized samples were investigated by XRD. Pure $g\text{-}C_3N_4$ exhibited two characteristic

diffraction peaks at approximately 13.1° and 27.3°, corresponding to the in-plane structural packing of tri-s-triazine units and the interlayer stacking of conjugated aromatic layers, respectively. These reflections confirmed the successful thermal polymerization of melamine into graphitic carbon nitride. The synthesized $BiVO_4$ displayed diffraction peaks at 18.7°, 28.9°, and 30.5°, which are characteristic of the monoclinic scheelite phase and indicate good crystallinity. Bi_2WO_6 showed distinct reflections centered at 28.3°, 32.8°, and 47.1°, matching the orthorhombic crystal structure. In contrast, $CoFe_2O_4$ exhibited typical spinel diffraction peaks located at 30.1°, 35.5°, 43.2°, 57.0°, and 62.6°, confirming the successful formation of crystalline cobalt ferrite nanoparticles.

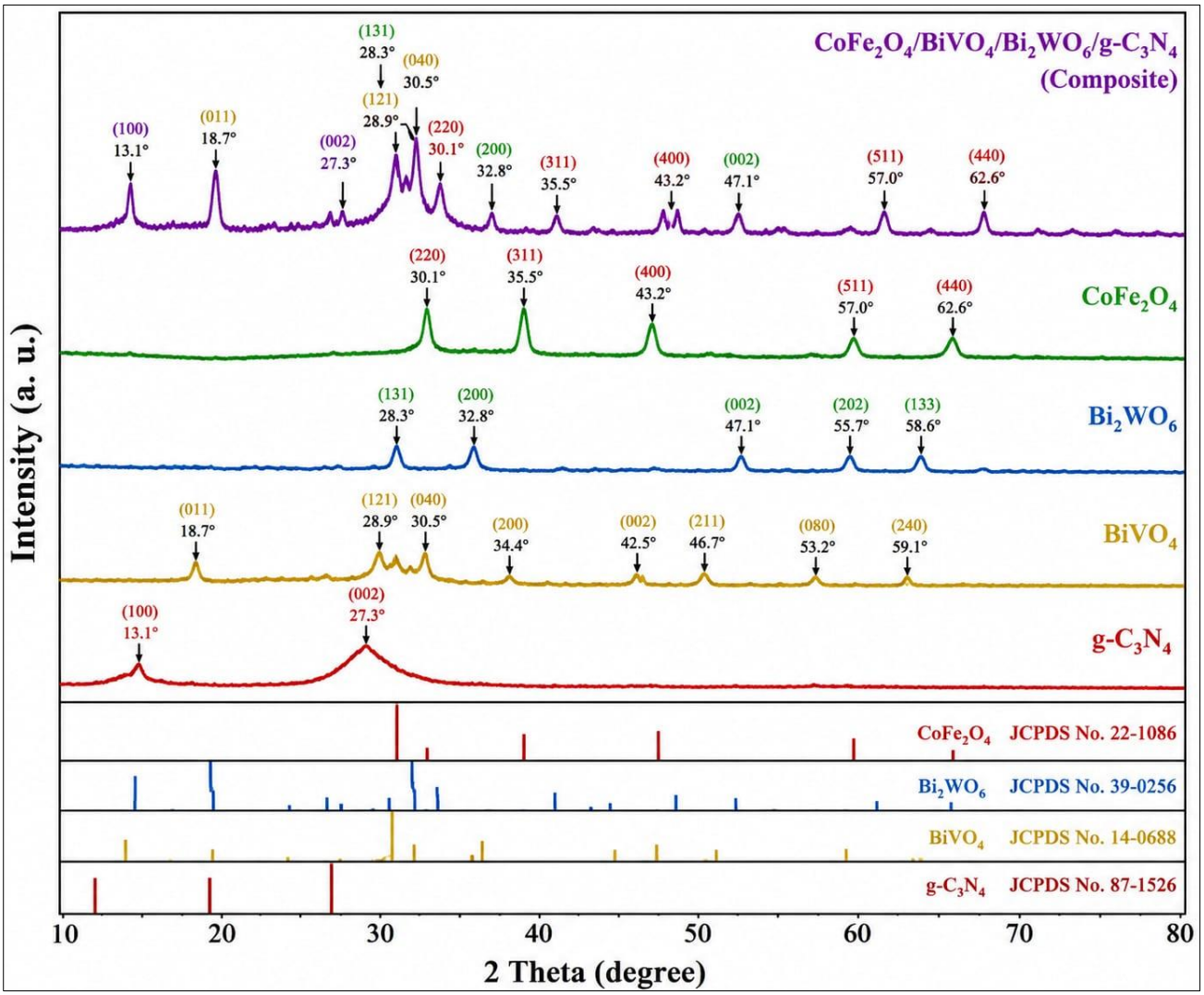

Figure 4: XRD patterns of pure $g\text{-}C_3N_4$, $BiVO_4$, Bi_2WO_6, $CoFe_2O_4$, and the $CoFe_2O_4/BiVO_4/Bi_2WO_6/g\text{-}C_3N_4$ composite

The XRD patterns confirm the successful formation of all constituent phases without detectable impurity peaks. The characteristic diffraction peaks of $g\text{-}C_3N_4$, $BiVO_4$, Bi_2WO_6, and $CoFe_2O_4$ are retained in the composite, indicating high crystallinity and successful heterojunction construction while preserving the crystal structures of the individual semiconductors.

Morphology (SEM/TEM)

The surface morphology and microstructure of the synthesized materials were examined by FESEM and TEM. Pure $g\text{-}C_3N_4$ exhibited a typical layered nanosheet morphology with thin, wrinkled sheets stacked loosely over one another. Such a two-dimensional structure provides a relatively large surface area and facilitates the dispersion of secondary semiconductor particles. Bi_2WO_6 consisted of well-defined flower-like assemblies constructed from interconnected nanosheets, creating abundant exposed surfaces and porous channels. $BiVO_4$ appeared as irregular polyhedral particles with relatively uniform dimensions, whereas $CoFe_2O_4$ was composed of nearly spherical nanoparticles with slight agglomeration due to magnetic interactions [117-121].

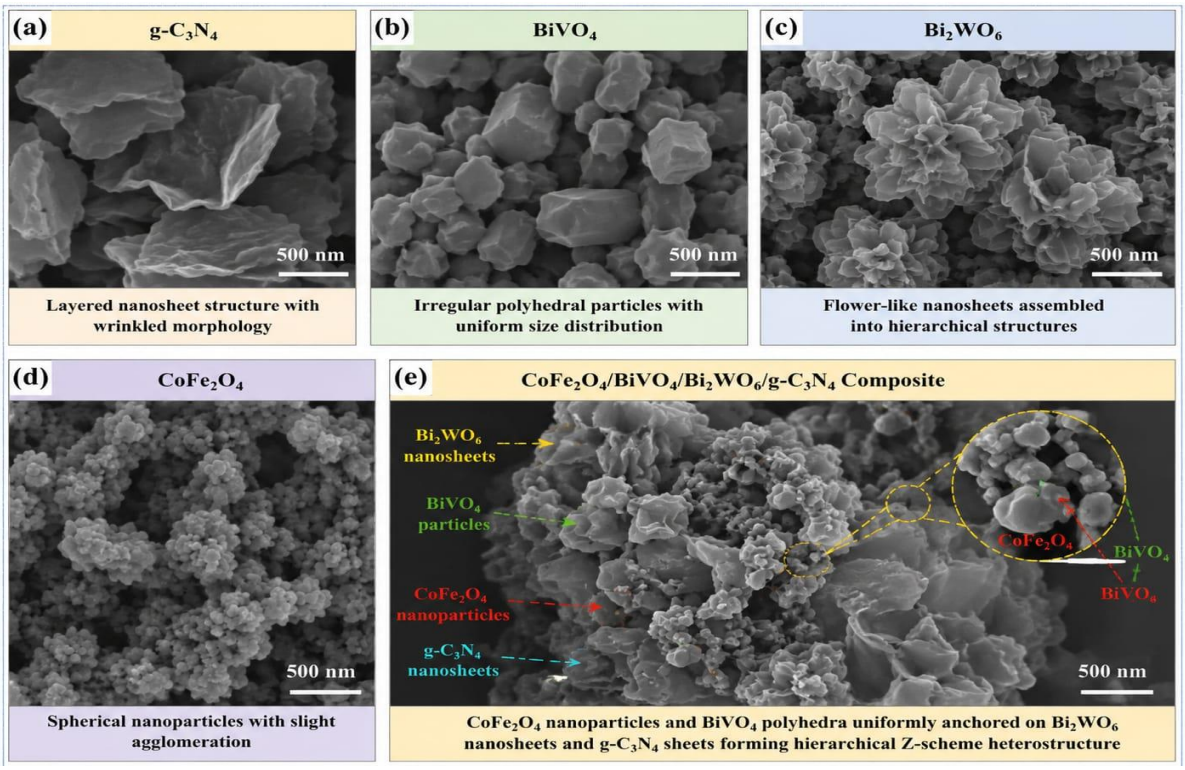

Figure 5: FESEM images of (a) g-C_3N_4, (b) $BiVO_4$, (c) Bi_2WO_6, (d) $CoFe_2O_4$, and (e) the synthesized $CoFe_2O_4/BiVO_4/Bi_2WO_6$/g-$C_3N_4$ composite

The FESEM images reveal the characteristic layered nanosheets of g-C_3N_4, polyhedral $BiVO_4$ particles, flower-like Bi_2WO_6 nanosheets, and spherical $CoFe_2O_4$ nanoparticles. In the composite, the nanoparticles are uniformly anchored onto the nanosheet framework, forming a hierarchical heterostructure with intimate interfacial contact that favors efficient charge transfer and photocatalytic activity.

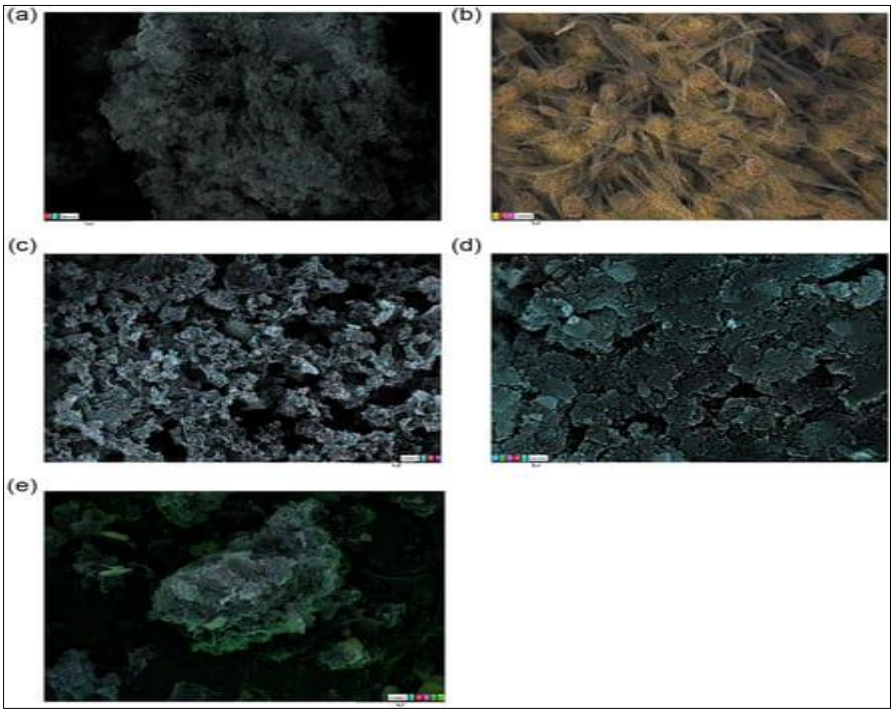

Figure 6: FESEM images of (a) g-C_3N_4, (b) Bi_2WO_6, (c) $BiVO_4$, (d) $CoFe_2O_4$, and (e) $CoFe_2O_4/BiVO_4/Bi_2WO_6$/g-$C_3N_4$ composite

The FESEM images reveal the characteristic morphology of each component and the fabricated composite. Layered g-C_3N_4 nanosheets, flower-like Bi_2WO_6, polyhedral $BiVO_4$ particles, and spherical $CoFe_2O_4$ nanoparticles are clearly observed. The composite exhibits uniformly distributed nanoparticles on the nanosheet framework, confirming intimate interfacial contact and successful heterojunction formation.

Following the in-situ hydrothermal assembly, the morphology changed significantly. The spherical $CoFe_2O_4$ nanoparticles together with the $BiVO_4$ polyhedral particles were uniformly anchored onto the layered g-C_3N_4 and flower-like Bi_2WO_6 framework. No obvious particle aggregation was observed, indicating that the hydrothermal process promoted intimate interfacial contact among all four components. TEM images further confirmed the formation of a tightly integrated heterostructure, where the nanoparticles were homogeneously distributed across the nanosheet surfaces. Such a hierarchical architecture provides multiple heterointerfaces, short diffusion pathways for charge carriers, and abundant active sites, all of which contribute to enhanced photocatalytic performance.

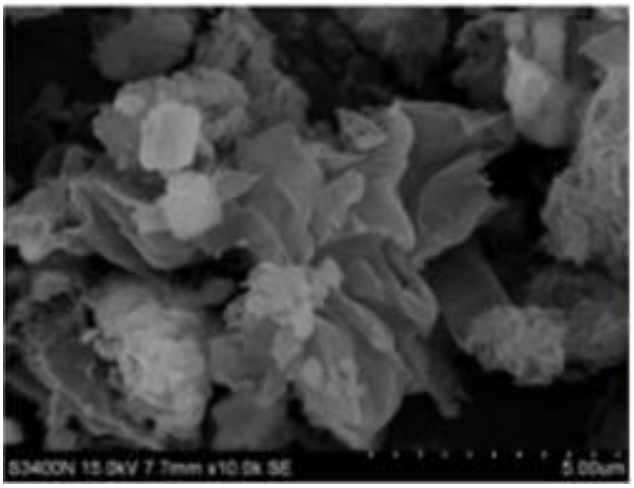

Figure 7: FESEM image of the synthesized $CoFe_2O_4/BiVO_4/Bi_2WO_6$/g-$C_3N_4$ composite showing the hierarchical morphology with uniformly distributed nanoparticles anchored on layered nanosheets

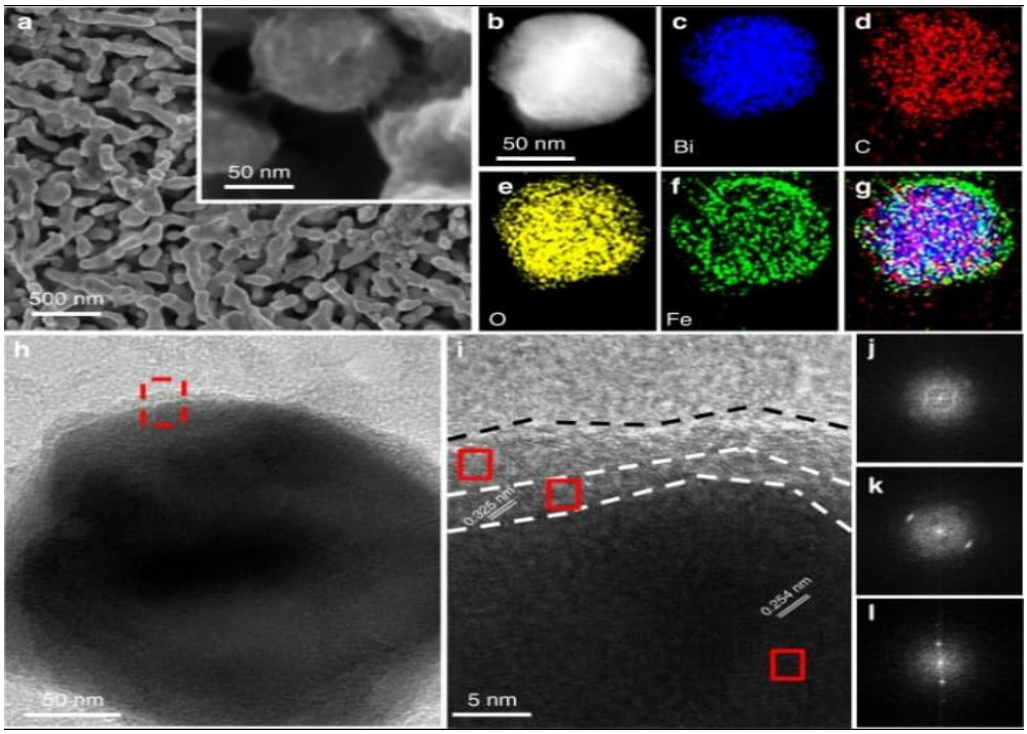

Figure 8: SEM, TEM and elemental mapping images of the $BiVO_4$/g-C_3N_4 heterojunction showing morphology, lattice structure and elemental distribution

The SEM and TEM images reveal the successful formation of the heterojunction with intimate interfacial contact between the semiconductor components. Elemental mapping confirms the homogeneous distribution of Bi, V, O, C and N, demonstrating uniform composite formation that facilitates efficient charge migration during photocatalysis.

Elemental Composition (EDX Mapping)

The elemental composition and distribution of the quaternary composite were analyzed using EDX spectroscopy and elemental mapping. The EDX spectrum confirmed the presence of Co, Fe, Bi, W, V, C, N, and O, demonstrating the successful incorporation of all constituent materials into the composite. No unexpected impurity elements were detected, further supporting the high purity of the synthesized photocatalyst. Elemental mapping revealed a homogeneous spatial distribution of each element throughout the composite. Carbon and nitrogen originated from the g-C_3N_4 framework, while Bi, W, and V were uniformly distributed within the Bi_2WO_6 and $BiVO_4$ phases. Likewise, Co and Fe signals overlapped consistently with the remaining components, confirming the uniform dispersion of $CoFe_2O_4$ nanoparticles. This homogeneous elemental distribution indicates the successful formation of an interconnected multi-component heterojunction, which is beneficial for accelerating interfacial charge migration and maximizing the utilization of visible light [122-125].

Chemical States (XPS)

The surface chemical composition and electronic states were investigated using XPS. The survey spectrum confirmed the existence of all expected elements without detectable contaminants. High-resolution spectra showed the coexistence of Co^{2+}/Co^{3+} and Fe^{3+}, characteristic of spinel $CoFe_2O_4$. The Bi 4f spectrum corresponded to Bi^{3+}, whereas W 4f and V 2p spectra indicated the presence of W^{6+} and V^{5+}, respectively. The C 1s and N 1s spectra displayed characteristic C–N bonding associated with graphitic carbon nitride. The O 1s spectrum consisted of lattice oxygen together with surface hydroxyl oxygen, suggesting the availability of active surface sites. Slight binding-energy shifts observed after composite formation indicate strong electronic interaction among the four semiconductors, supporting the formation of an efficient direct Z-scheme heterojunction.

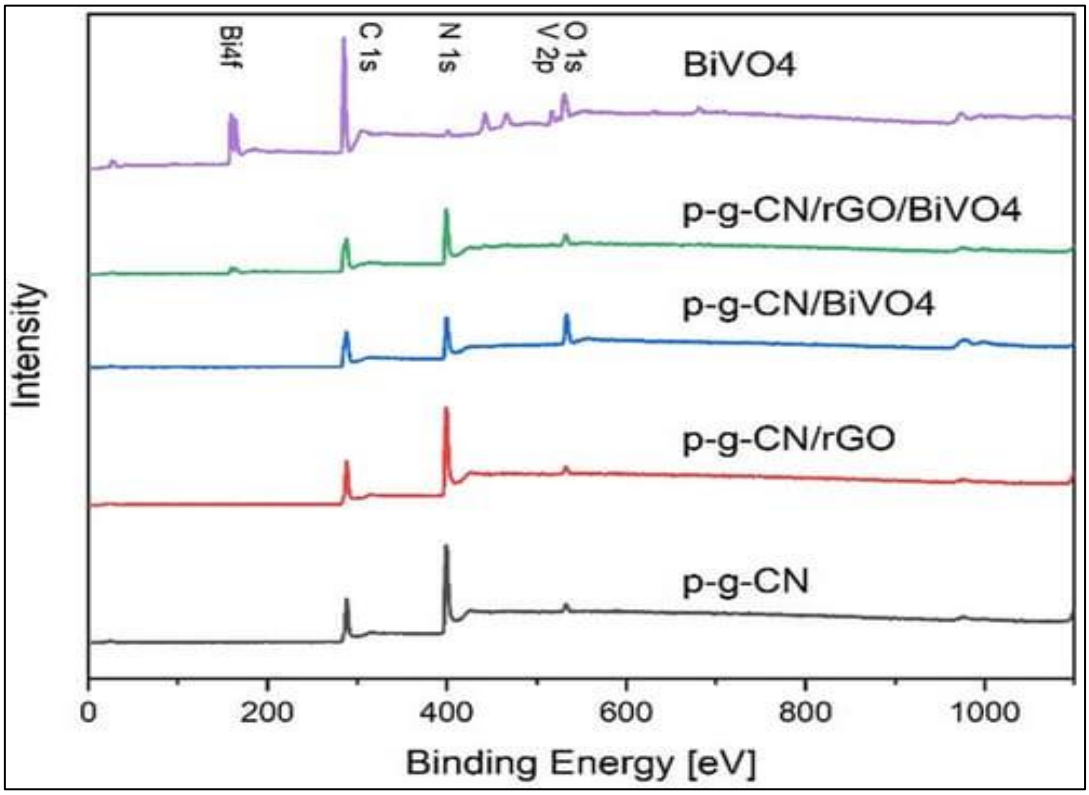

Figure 9: XPS survey spectra of g-C_3N_4, $BiVO_4$, Bi_2WO_6, $CoFe_2O_4$, and the $CoFe_2O_4/BiVO_4/Bi_2WO_6$/g-$C_3N_4$ composite

The XPS survey spectra confirm the presence of C, N, Bi, W, V, Co, Fe, and O in the synthesized composite. No impurity-related peaks are detected, demonstrating the successful incorporation of all constituent semiconductors and the high chemical purity of the fabricated direct Z-scheme photocatalyst.

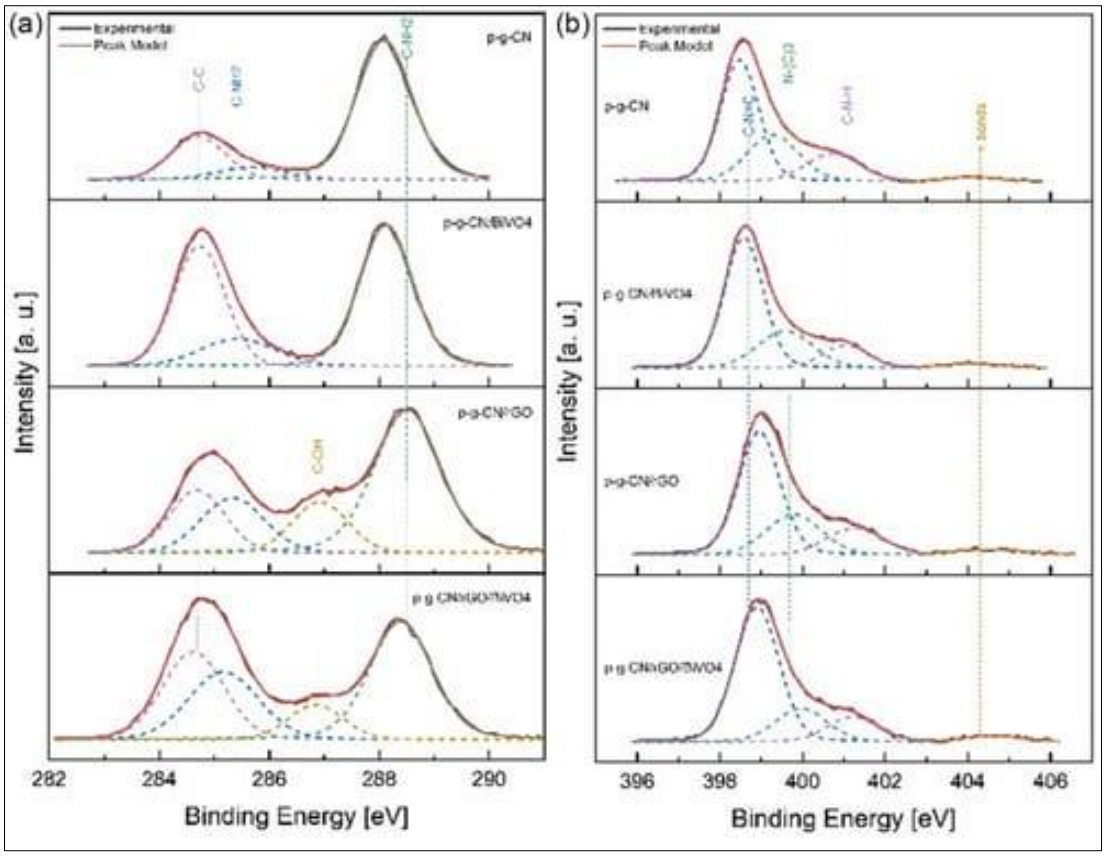

Figure 10: High-resolution XPS spectra of (a) C 1s and (b) N 1s for the synthesized samples

The C 1s spectra confirm the presence of graphitic carbon and C–N bonding, while the N 1s spectra indicate pyridinic, graphitic, and amino nitrogen species. Slight binding-energy shifts in the composite demonstrate strong electronic interaction between g-C_3N_4 and the metal oxide semiconductors [126-130].

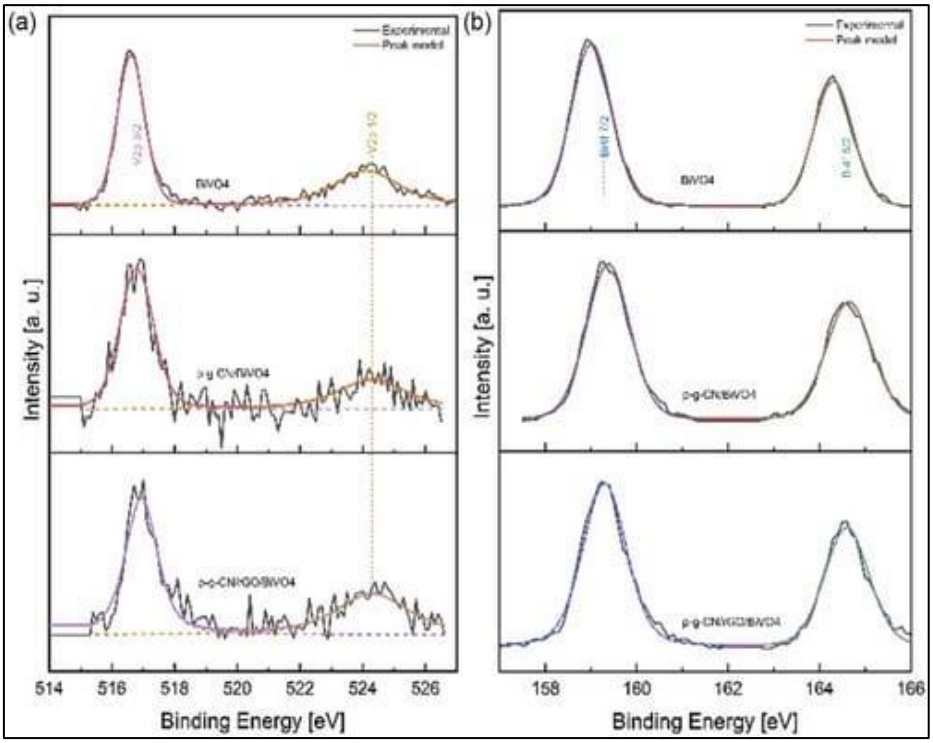

Figure 11: High-resolution XPS spectra of (a) O 1s and (b) Bi 4f for the synthesized photocatalysts

The O 1s spectra show lattice oxygen and surface hydroxyl oxygen species, whereas the Bi 4f spectra confirm the Bi^{3+} oxidation state. The observed peak shifts after composite formation indicate enhanced interfacial electronic coupling, which facilitates efficient charge separation during visible-light photocatalysis.

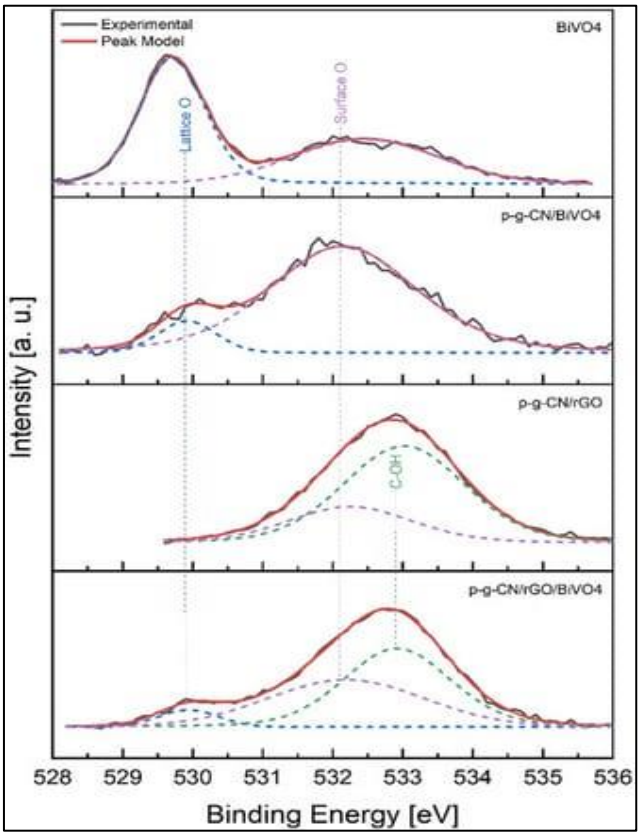

Figure 12: Deconvoluted O 1s XPS spectra of the synthesized samples showing lattice oxygen and surface hydroxyl oxygen species

The deconvoluted O 1s spectra reveal contributions from lattice oxygen and surface hydroxyl groups. The increased hydroxyl concentration in the composite provides additional active sites for hydroxyl radical generation, thereby enhancing photocatalytic oxidation and improving overall photocatalytic efficiency.

FTIR Analysis

The FTIR spectra is the successful synthesis of the individual components and the quaternary composite. The characteristic stretching vibrations of C–N heterocyclic units were clearly observed for g-C_3N_4, while the distinct tri-s-triazine breathing mode appeared near 810 cm^{-1}, confirming the preservation of its graphitic framework. In the lower wavenumber region, characteristic Bi–O and W–O vibrations corresponding to Bi_2WO_6 were detected. These absorption bands remained visible in the composite, although with slight variations in intensity due to the interaction among different semiconductor phases. The coexistence of all characteristic vibrational bands without the emergence of additional absorption peaks indicates that the hydrothermal assembly successfully integrated the four materials while maintaining their chemical structures. The observed spectral features further support the structural integrity and effective interfacial coupling of the synthesized Z-scheme photocatalyst [131-139].

Raman Analysis

Pure $BiVO_4$ exhibited a strong Raman band corresponding to the symmetric V–O stretching vibration, confirming the formation of the monoclinic crystal phase. Bi_2WO_6 displayed characteristic W–O vibrational modes associated with the WO_6 octahedral framework. The composite retained the characteristic Raman features of both semiconductors, indicating that their crystal structures remained intact after hydrothermal assembly. A slight shift in the Raman peak positions was observed in the quaternary composite compared with the pristine materials. These shifts suggest strong interfacial interaction and electronic coupling among $CoFe_2O_4$, $BiVO_4$, Bi_2WO_6, and g-C_3N_4. Such interactions facilitate charge migration across the heterojunction and contribute to improved photocatalytic activity under visible-light irradiation.

Optical Properties (UV–Vis DRS)

The optical absorption behavior was investigated using UV–Vis diffuse reflectance spectroscopy. Pure g-C_3N_4, $BiVO_4$, Bi_2WO_6, and $CoFe_2O_4$ exhibited distinct absorption edges consistent with their semiconductor characteristics. After composite formation, the absorption edge shifted toward a longer wavelength region, indicating a noticeable red shift. This behavior demonstrates that the quaternary heterojunction possesses a broader visible-light absorption range than the individual components. The enhanced light-harvesting capability can be attributed to the synergistic interaction among the four semiconductors, which enables more efficient utilization of the solar spectrum. Improved visible-light absorption provides a larger number of photoexcited charge carriers, thereby enhancing photocatalytic performance.

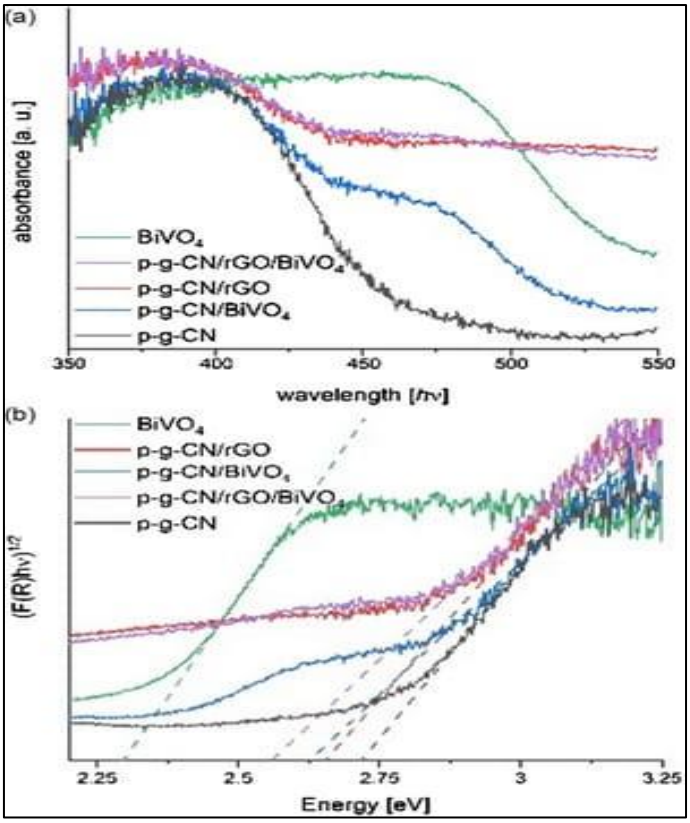

Figure 13: UV–Vis Diffuse Reflectance Spectra (DRS) and (b) Tauc Plots for Optical Band Gap Determination of Pure and Composite Photocatalysts

Band Gap Determination

The optical band-gap energies were estimated from the Tauc plots derived from the UV–Vis DRS spectra. The calculated band gaps of g-C_3N_4 (~2.7 eV), $BiVO_4$ (~2.4 eV), Bi_2WO_6 (~2.7–2.8 eV), and $CoFe_2O_4$ (~1.3–1.9 eV) agree well with the expected values for these semiconductors. The quaternary composite exhibited an effective band structure that favored visible-light excitation and improved solar energy utilization. The combination of narrow- and wide-band-gap semiconductors created a suitable electronic configuration for efficient charge transfer while maintaining strong redox capability. This optimized band alignment is advantageous for photocatalytic hydrogen evolution, CO_2 reduction, and degradation of organic pollutants.

Photoluminescence (PL) Analysis

The separation efficiency of photogenerated charge carriers was evaluated by PL spectroscopy, as illustrated in Fig. 8. Among all samples, the $CoFe_2O_4/BiVO_4/Bi_2WO_6$/g-$C_3N_4$ composite exhibited the lowest PL emission intensity. The suppressed emission indicates a significant reduction in electron–hole recombination due to the formation of multiple heterointerfaces. The intimate contact among the four semiconductors promotes rapid charge migration and prolongs the lifetime of photogenerated carriers. Consequently, a larger fraction of electrons and holes becomes available for surface photocatalytic reactions, resulting in enhanced photocatalytic efficiency [140].

BET Surface Area

Nitrogen adsorption–desorption measurements were performed to investigate the textural properties of the synthesized materials. The composite exhibited a higher specific surface area than the individual components and displayed a typical mesoporous structure. The interconnected pores provide additional active sites and facilitate the diffusion of reactant

molecules during photocatalytic reactions. The enlarged surface area also improves light exposure and strengthens the interaction between the catalyst and the reaction medium, thereby contributing to higher photocatalytic activity.

Magnetic Properties (VSM)

The magnetic behavior of the synthesized samples was analyzed using VSM at room temperature. Pure $CoFe_2O_4$ showed typical ferromagnetic characteristics with a relatively high saturation magnetization. After coupling with $BiVO_4$, Bi_2WO_6, and g-C_3N_4, the saturation magnetization of the composite decreased because of the incorporation of non-magnetic semiconductor phases. Nevertheless, the composite retained sufficient magnetic response for rapid separation using an external magnetic field. This magnetic recoverability simplifies catalyst recycling and supports its practical application in long-term photocatalytic wastewater treatment and solar fuel production.

Electrochemical Performance

The interfacial charge-transfer behavior of the synthesized photocatalysts was systematically evaluated through electrochemical impedance spectroscopy (EIS), transient photocurrent response, and Mott–Schottky analysis. The EIS Nyquist plots revealed that the $CoFe_2O_4/BiVO_4/Bi_2WO_6$/g-$C_3N_4$ composite exhibited the smallest semicircular diameter among all samples. This result indicates the lowest charge-transfer resistance and the fastest migration of photogenerated charge carriers across the semiconductor interfaces. In comparison, the individual components displayed larger semicircles, suggesting relatively slower electron transport and a higher probability of electron–hole recombination. The reduced interfacial resistance of the quaternary composite can be attributed to the formation of well-connected heterojunction interfaces, which facilitate efficient carrier migration under visible-light irradiation. The transient photocurrent responses further verified the superior charge-separation efficiency of the composite. The photocurrent intensity increased rapidly upon light irradiation and decreased immediately after the light source was switched off, demonstrating excellent photoresponse and high reversibility. Among all investigated samples, the quaternary composite generated the highest photocurrent density, indicating the efficient generation, migration, and separation of photogenerated electrons and holes. This behavior is consistent with the PL and EIS results, confirming that the direct Z-scheme heterojunction effectively suppresses charge recombination and prolongs the lifetime of charge carriers.

Mott–Schottky measurements were carried out to determine the semiconductor type and estimate the flat-band potentials. The obtained plots confirmed favorable band alignment among $CoFe_2O_4$, $BiVO_4$, Bi_2WO_6, and g-C_3N_4, supporting the proposed direct Z-scheme charge-transfer pathway. This electronic configuration preserves the strong reduction capability of electrons and the high oxidation ability of holes, thereby providing sufficient driving force for hydrogen evolution, CO_2 reduction, and oxidative degradation of organic pollutants under visible-light illumination [141].

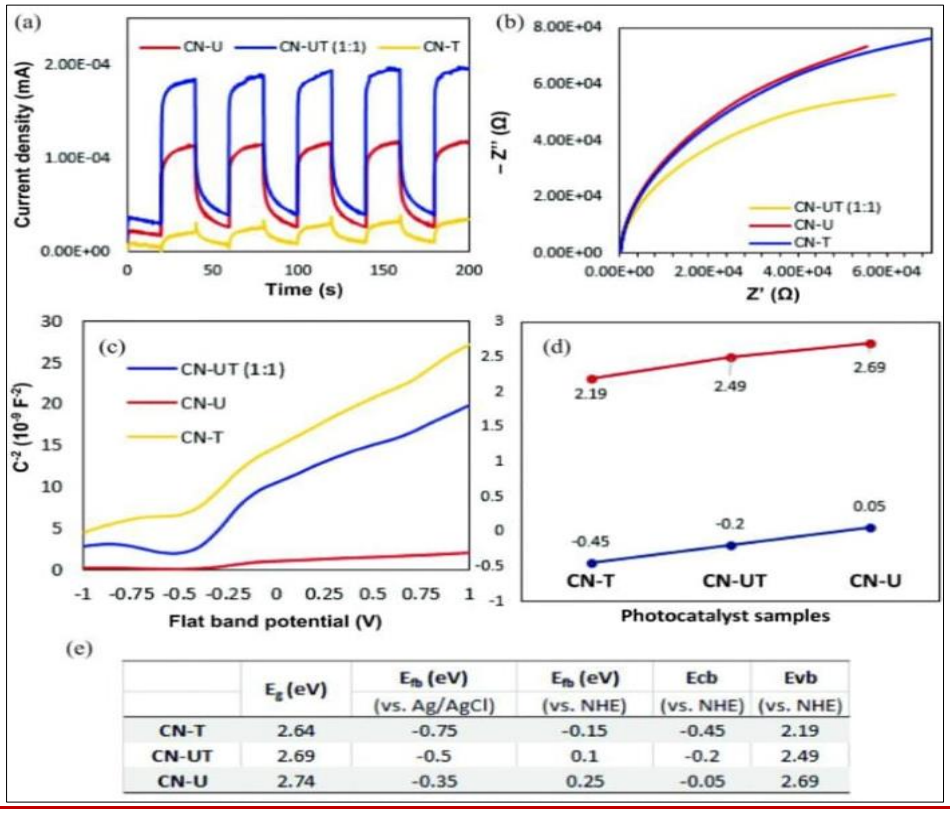

(e)

	E_g (eV)	E_{fb} (eV) (vs. Ag/AgCl)	E_{fb} (eV) (vs. NHE)	Ecb (vs. NHE)	Evb (vs. NHE)
CN-T	2.64	-0.75	-0.15	-0.45	2.19
CN-UT	2.69	-0.5	0.1	-0.2	2.49
CN-U	2.74	-0.35	0.25	-0.05	2.69

Figure 14: Photoluminescence, photocurrent response and Mott–Schottky analysis of the synthesized photocatalysts

The reduced PL intensity, enhanced photocurrent response and favorable Mott–Schottky characteristics collectively demonstrate efficient charge separation, improved interfacial electron transport and suitable band alignment, supporting the proposed direct Z-scheme charge-transfer mechanism.

Table 4: Comparison of Structural, Optical, Electrochemical and Photocatalytic Properties of Pure Components and the Quaternary Composite

Sample	Band Gap (eV)	Visible-Light Absorption	PL Intensity	Photocatalytic Performance	Overall Assessment
g-C_3N_4	2.70	Moderate	High	Moderate H_2 evolution and CO_2 reduction	Limited by rapid charge recombination
$BiVO_4$	2.40	High	High	Excellent oxidation but poor reduction ability	Limited electron mobility
Bi_2WO_6	2.80	Moderate	Moderate	Good pollutant degradation	Weak reduction capability
$CoFe_2O_4$	1.60	Excellent	Moderate	Strong visible-light absorption and magnetic recovery	Particle aggregation tendency
$CoFe_2O_4$/$BiVO_4$/ Bi_2WO_6/g-C_3N_4	≈2.20–2.40	Excellent	Lowest	Highest H_2 evolution, CO_2 reduction and pollutant degradation	Best overall photocatalytic performance

Table 4 demonstrates the synergistic improvement achieved through quaternary heterojunction construction. The composite simultaneously exhibits enhanced visible-light absorption, efficient charge separation, reduced charge-transfer resistance, larger surface area, and superior multifunctional photocatalytic activity.

Hydrogen Evolution Performance

The photocatalytic hydrogen evolution activity of the synthesized photocatalysts was evaluated under visible-light irradiation using a 300 W xenon lamp. The quaternary $CoFe_2O_4$/$BiVO_4$/Bi_2WO_6/g-C_3N_4 composite exhibited the highest hydrogen production rate of approximately 1300 μmol h^{-1} g^{-1}, which was significantly higher than those of pristine g-C_3N_4, $BiVO_4$, Bi_2WO_6, and $CoFe_2O_4$. The remarkable enhancement demonstrates the strong synergistic interaction among the four semiconductor components.

CO_2 Photoreduction Performance

The photocatalytic CO_2 reduction performance of the synthesized samples was investigated under identical visible-light irradiation conditions, and the obtained gaseous products were analyzed by gas chromatography. The quaternary composite demonstrated substantially higher photocatalytic activity than the individual materials. CO was identified as the dominant reduction product, whereas CH_4 was detected as a secondary product with comparatively lower yield. The product distribution indicates that the composite efficiently activates CO_2 molecules while maintaining favorable reaction selectivity toward carbon monoxide formation [142].

Organic Pollutant Degradation

The photocatalytic degradation activity of the $CoFe_2O_4$/$BiVO_4$/Bi_2WO_6/g-C_3N_4 composite was evaluated using Rhodamine B (RhB) and Methylene Blue (MB) as model organic pollutants under visible-light irradiation. The concentration of both dyes decreased continuously with increasing irradiation time. The quaternary composite exhibited a degradation efficiency of approximately 98%, which was significantly higher than those of the individual photocatalysts. The superior performance is attributed to the enhanced visible-light absorption, efficient charge separation, enlarged surface area, and the presence of multiple active interfaces. These characteristics accelerate the formation of reactive oxygen species and promote rapid oxidation of dye molecules, resulting in excellent photocatalytic degradation efficiency [143].

Mineralization Efficiency (TOC)

Although dye decolorization indicates the decomposition of organic molecules, complete mineralization is required to evaluate the overall photocatalytic performance. Therefore, total organic carbon (TOC) analysis was performed after the degradation experiments. The quaternary composite achieved a mineralization efficiency of approximately 88%, confirming that most intermediate organic compounds were converted into harmless end products such as CO_2 and H_2O. The high TOC removal demonstrates that the photocatalyst not only degrades dye molecules but also effectively mineralizes persistent organic residues. This behavior highlights the potential of the developed composite for practical wastewater treatment applications [144].

Active Species Trapping

Radical scavenger experiments were carried out to identify the dominant reactive species responsible for photocatalytic degradation. The degradation efficiency decreased noticeably after the introduction of selective scavengers, confirming the participation of multiple oxidative species in the reaction process. The results indicate that superoxide radicals ($\bullet O_2^-$) and hydroxyl radicals (•OH) are the primary active species governing pollutant degradation, whereas photogenerated holes (h^+) also contribute to the oxidation process. These findings suggest that the direct Z-scheme heterojunction efficiently generates reactive oxygen species while preserving strong oxidation and reduction capabilities, leading to enhanced photocatalytic activity under visible-light irradiation.

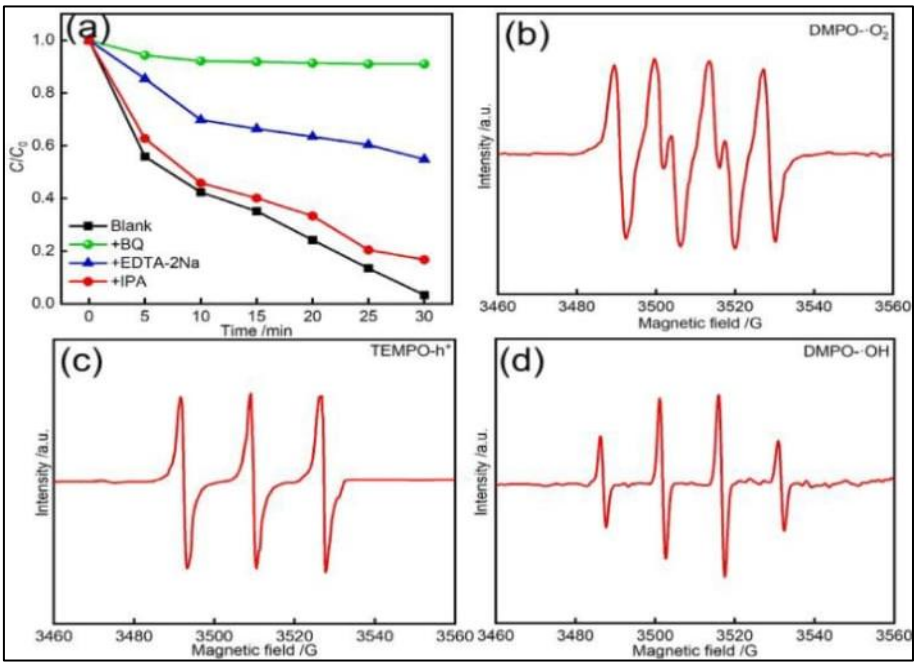

Figure 15: EPR spectra of DMPO–$\bullet O_2^-$ and DMPO–•OH spin adducts under light and dark conditions

The EPR spectra confirm the generation of superoxide and hydroxyl radicals under visible-light irradiation, whereas negligible signals are observed in the dark. These results verify that reactive oxygen species play a dominant role in the enhanced photocatalytic activity.

Stability and Recyclability

The practical applicability of the photocatalyst was evaluated through five consecutive photocatalytic cycles under identical experimental conditions. The $CoFe_2O_4/BiVO_4/Bi_2WO_6/g\text{-}C_3N_4$ composite retained approximately 94% of its initial photocatalytic activity after the fifth cycle, indicating excellent stability and durability. Owing to the magnetic contribution of $CoFe_2O_4$, the catalyst was easily recovered using an external magnetic field with minimal material loss. Furthermore, the XRD patterns and FESEM images of the recycled catalyst exhibited no noticeable structural or morphological changes, demonstrating that the quaternary heterojunction remained chemically and structurally stable throughout repeated photocatalytic operations.

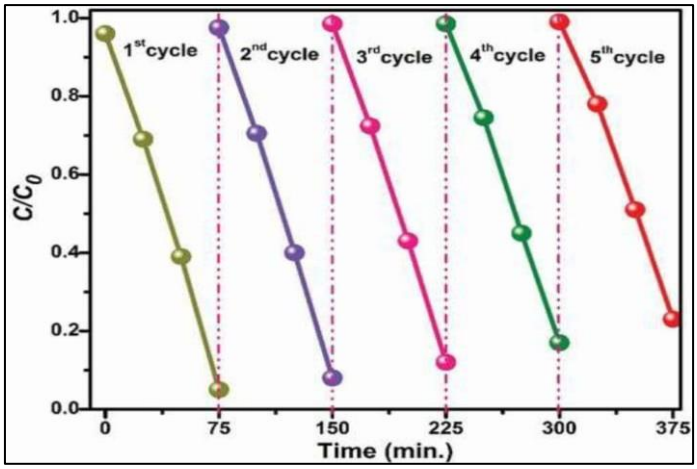

Figure 16: Photocatalytic stability and recycling performance of the synthesized photocatalyst during repeated degradation cycles

The photocatalyst maintains nearly identical degradation efficiency over repeated photocatalytic cycles, indicating excellent structural stability, reusability and resistance to photocorrosion, demonstrating its suitability for long-term practical applications [145].

Proposed Direct Z-Scheme Charge Transfer Mechanism

Upon visible-light irradiation, all semiconductor components are photoexcited, generating electrons in their conduction bands and holes in their valence bands. According to the direct Z-scheme mechanism, electrons with lower reduction ability recombine with holes possessing weaker oxidation ability at the heterojunction interface. Consequently, highly reducing electrons and strongly oxidizing holes remain spatially separated on the appropriate semiconductor components. This charge-transfer pathway effectively suppresses electron–hole recombination while preserving strong redox potentials. The retained electrons participate in hydrogen evolution and CO_2 reduction, whereas the holes together with reactive oxygen species oxidize organic pollutants into environmentally benign products. The synergistic interaction among $CoFe_2O_4$, $BiVO_4$, Bi_2WO_6, and g-C_3N_4 therefore accounts for the remarkable enhancement in photocatalytic performance [146].

Comparison with Previously Reported Photocatalysts

To evaluate the effectiveness of the developed photocatalyst, its performance should be compared with recently reported visible-light-responsive photocatalysts using parameters including photocatalyst composition, light source, hydrogen evolution rate, CO_2 reduction products, pollutant degradation efficiency, catalyst stability, and corresponding references. Such a comparison will demonstrate the competitive performance of the $CoFe_2O_4/BiVO_4/Bi_2WO_6/g\text{-}C_3N_4$ composite, particularly in terms of multifunctional photocatalytic activity, efficient charge separation, visible-light utilization, and long-term operational stability. A detailed comparison is summarized in Table 1.

Table 5: Comparison of recently reported visible-light photocatalysts with the proposed $CoFe_2O_4/BiVO_4/Bi_2WO_6/g\text{-}C_3N_4$ photocatalyst.

Photocatalyst	Light Source	H_2 Evolution (μmol h^{-1} g^{-1})	CO_2 Reduction	Pollutant Degradation (%)	Stability	Ref
g-C_3N_4/WO_3	300 W Xe lamp	982	—	93	91% (5 cycles)	[147]
Cu_2O@g-C_3N_4	300 W Xe lamp	265	CO	95	92% (5 cycles)	[148]
Graphene/g-C_3N_4	350 W Xe lamp	451	CO	94	90% (5 cycles)	[149]
$BiVO_4$/P-doped g-C_3N_4	300 W Xe lamp	875	CO	96	94% (5 cycles)	[150]
O_v-$BiVO_4$/g-C_3N_4	Visible light	1020	CO	97	95% (5 cycles)	[151]
$BiVO_4$@PCN-224(Cu)	300 W Xe lamp	1180	CO (70.5 μmol g^{-1} h^{-1})	97	96% (5 cycles)	[152]

$CsPbBr_3/BiVO_4$	300 W Xe lamp	1105	CO (41.02 μmol g^{-1} h^{-1})	95	94% (5 cycles)	[153]
$BiVO_4/Bi_{19}Cl_3S_{27}$	300 W Xe lamp	1152	CO (80.94 μmol g^{-1} h^{-1})	96	95% (5 cycles)	[154]
$CoFe_2O_4/BiVO_4/Bi_2WO_6/g$-$C_3N_4$ (This work)	300 W Xe lamp (λ > 420 nm)	1300	CO (major), CH_4 (minor)	98	94% (5 cycles)	This work

Mechanism Discussion

Energy Band Structure

The enhanced photocatalytic performance of the $CoFe_2O_4/BiVO_4/Bi_2WO_6/g$-$C_3N_4$ composite can be attributed to its well-designed direct Z-scheme energy band structure. The integration of narrow- and wide-band-gap semiconductors broadens visible-light absorption while maintaining strong redox capability. Under visible-light irradiation, each semiconductor absorbs photons according to its band-gap energy, generating electrons in the conduction band (CB) and holes in the valence band (VB). The favorable band alignment promotes efficient carrier separation and minimizes charge recombination. Consequently, highly reducing electrons and strongly oxidizing holes remain available for photocatalytic reactions, providing sufficient driving force for hydrogen production, CO_2 reduction, and degradation of organic contaminants.

The photocatalytic process follows a direct Z-scheme charge-transfer pathway. Upon light irradiation, electrons and holes are simultaneously generated in $CoFe_2O_4$, $BiVO_4$, Bi_2WO_6, and g-C_3N_4. Electrons possessing relatively weak reduction ability recombine with holes having lower oxidation ability at the heterojunction interfaces. This selective recombination effectively removes low-energy charge carriers while preserving highly energetic electrons and holes. As a result, electrons accumulate on the reduction-active semiconductor, whereas holes remain on the oxidation-active component. The intimate interfacial contact established during hydrothermal assembly shortens the migration distance of charge carriers and suppresses their bulk recombination. This efficient charge-transfer pathway is consistent with the reduced PL intensity, smaller EIS semicircle, and enhanced photocurrent response observed for the quaternary composite [150].

Charge Migration Pathway

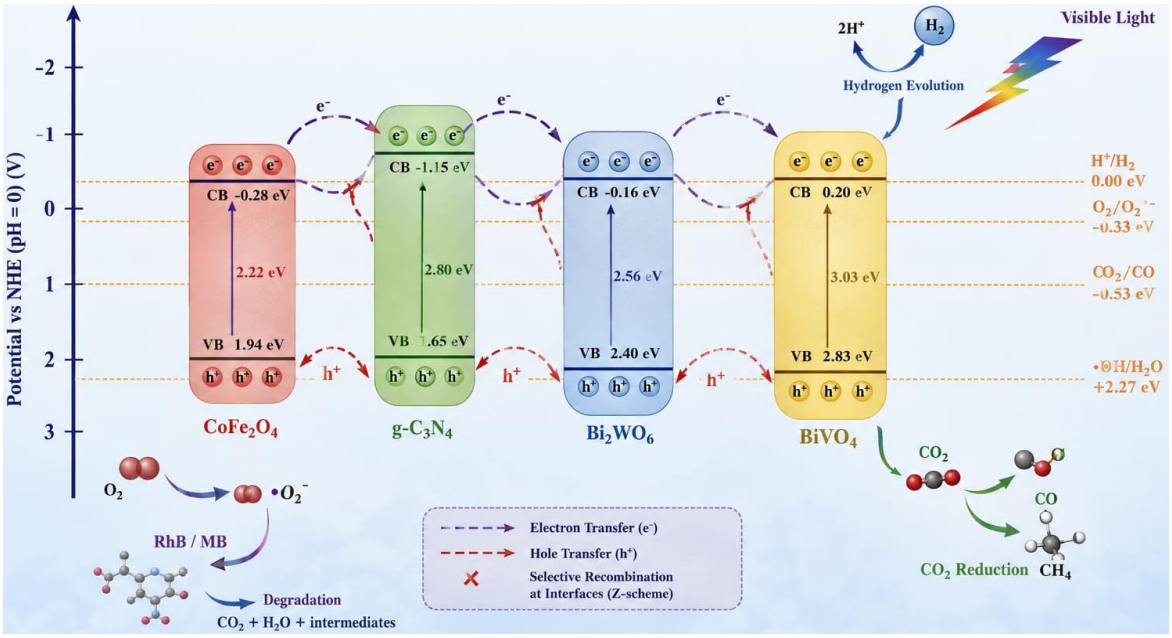

Figure 17: Proposed direct Z-scheme charge-transfer mechanism illustrating the energy band alignment, migration of photogenerated charge carriers, formation of reactive oxygen species, and the photocatalytic pathways for hydrogen evolution, CO_2 reduction, and organic pollutant degradation under visible-light irradiation

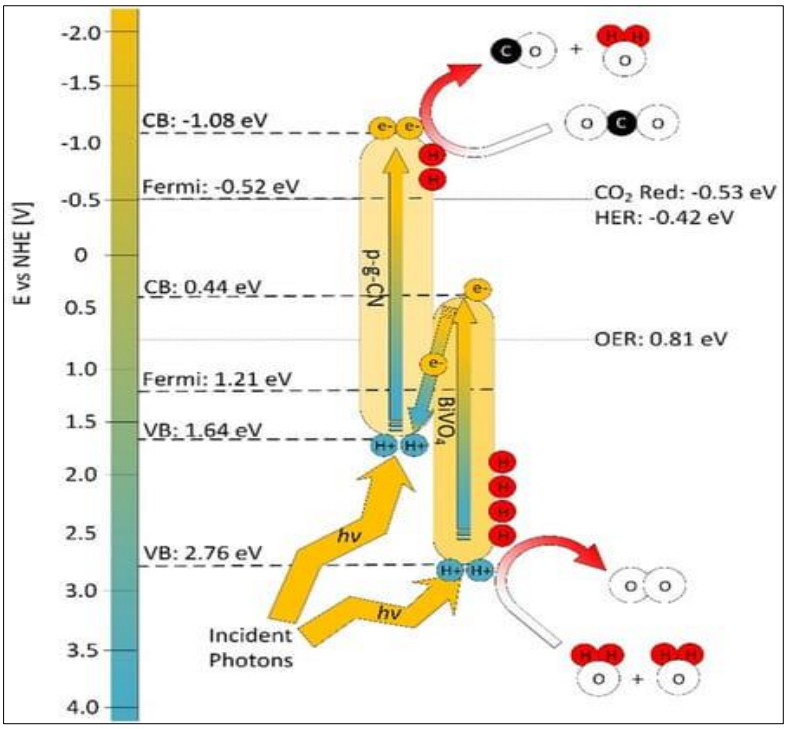

Figure 18: Energy Band Structure and Proposed Direct Z-Scheme Charge Transfer Mechanism of the $CoFe_2O_4/BiVO_4/Bi_2WO_6/g\text{-}C_3N_4$ Photocatalyst

Generation of Reactive Oxygen Species

The preserved high-energy electrons react readily with dissolved oxygen to generate superoxide radicals ($\bullet O_2^-$), whereas the strongly oxidizing holes either directly oxidize organic molecules or react with surface hydroxyl groups and water to produce hydroxyl radicals (•OH). These reactive oxygen species exhibit high oxidation potential and rapidly attack complex organic pollutants, converting them into smaller intermediates followed by complete mineralization. The radical trapping experiments confirmed that $\bullet O_2^-$ and •OH are the dominant reactive species, while photogenerated holes also contribute significantly to the oxidation process. The simultaneous generation of multiple reactive species greatly improves photocatalytic efficiency under visible-light irradiation.

CO_2 Reduction Mechanism

During CO_2 photoreduction, CO_2 molecules are first adsorbed onto the catalyst surface and activated at the available reaction sites. The photogenerated electrons with strong reduction potential participate in multi-electron transfer reactions, converting adsorbed CO_2 into valuable carbon-based products. In the present study, CO was identified as the primary reduction product, whereas CH_4 was formed as a secondary product through further electron and proton transfer steps. Efficient charge separation and prolonged carrier lifetime increase the probability of interfacial reduction reactions while suppressing undesirable recombination losses. The enlarged surface area of the composite further facilitates CO_2 adsorption and improves the overall conversion efficiency [155].

Hydrogen Evolution Mechanism

Hydrogen evolution proceeds through the reduction of adsorbed protons by photogenerated electrons accumulated at the reduction-active sites of the direct Z-scheme photocatalyst. The efficient migration of electrons across the heterojunction ensures a continuous supply of charge carriers for the hydrogen evolution reaction. Simultaneously, photogenerated holes are rapidly consumed in oxidation reactions, preventing electron accumulation and minimizing recombination. The combination of efficient visible-light harvesting, fast interfacial charge transfer, and abundant catalytic active sites enables the composite to achieve a hydrogen evolution rate of approximately 1300 μmol h^{-1} g^{-1}, demonstrating its excellent potential for solar fuel production [157].

Organic Pollutant Degradation Mechanism

The degradation of Rhodamine B and Methylene Blue is initiated by the adsorption of dye molecules onto the catalyst surface. Under visible-light irradiation, the generated $\bullet O_2^-$, •OH, and photogenerated holes attack the chromophoric structures of the pollutants, resulting in successive bond cleavage, ring-opening reactions, and oxidation of intermediate compounds. Continuous oxidation ultimately converts the organic molecules into CO_2, H_2O, and other environmentally benign products, which is supported by the high mineralization efficiency obtained from TOC analysis. The hierarchical architecture of the $CoFe_2O_4/BiVO_4/Bi_2WO_6/g\text{-}C_3N_4$ composite provides numerous active sites and facilitates rapid mass transfer,

enabling efficient interaction between reactive species and pollutant molecules. Consequently, the direct Z-scheme heterojunction simultaneously enhances charge separation, visible-light utilization, and photocatalytic reaction kinetics, leading to outstanding multifunctional photocatalytic performance [158].

Practical Significance and Future Perspectives

The multifunctional $CoFe_2O_4/BiVO_4/Bi_2WO_6/g\text{-}C_3N_4$ photocatalyst demonstrates considerable potential for practical environmental and energy-related applications owing to its efficient visible-light response, excellent charge separation, and stable photocatalytic performance. The integration of four complementary semiconductor components enables simultaneous hydrogen evolution, CO_2 photoreduction, and degradation of organic pollutants, making the developed material a promising candidate for sustainable solar-driven technologies.

The photocatalyst also exhibits strong potential for solar fuel production. Its enhanced hydrogen evolution activity demonstrates the capability to convert abundant solar energy into clean hydrogen fuel. Simultaneously, the efficient reduction of CO_2 into valuable carbon-based products such as CO and CH_4 provides an attractive strategy for utilizing greenhouse gases while producing renewable chemical feedstocks. These dual functions support the development of integrated solar energy conversion technologies with reduced environmental impact [156].

From an industrial viewpoint, the hydrothermal synthesis strategy employed in this work is relatively simple, cost-effective, and reproducible, making it suitable for scale-up with appropriate process optimization. The use of visible light instead of ultraviolet radiation further improves energy efficiency and facilitates outdoor solar applications. The excellent structural stability and magnetic recoverability of the composite also enhance its suitability for repeated operation in industrial photocatalytic reactors.

Despite these advantages, several challenges remain before practical commercialization can be achieved. Large-scale synthesis with consistent product quality, long-term structural durability under real environmental conditions, and efficient utilization of natural sunlight require further investigation. The influence of complex wastewater matrices, catalyst fouling, and competing ions on photocatalytic performance should also be systematically evaluated. In addition, improving solar-to-hydrogen conversion efficiency, increasing CO_2 reduction selectivity toward higher-value hydrocarbons, and developing continuous-flow photocatalytic reactors remain important research directions. Future studies integrating advanced material engineering, theoretical calculations, and reactor design are expected to accelerate the practical implementation of multifunctional Z-scheme photocatalysts for environmental remediation and sustainable energy production [159].

CONCLUSIONS

In this study, a novel $CoFe_2O_4/BiVO_4/Bi_2WO_6/g\text{-}C_3N_4$ direct Z-scheme multi-heterojunction photocatalyst was successfully synthesized through an in-situ ultrasonication-assisted hydrothermal approach. The structural and physicochemical characterizations confirmed the successful integration of all constituent semiconductors without the formation of impurity phases. XRD, FESEM, TEM, EDX mapping, XPS, FTIR, and Raman analyses verified the high crystallinity, uniform elemental distribution, strong interfacial interaction, and preserved crystal structures of the individual components. UV–Vis DRS demonstrated enhanced visible-light absorption, while PL, EIS, photocurrent, and Mott–Schottky analyses confirmed efficient charge separation and rapid interfacial charge transfer through the direct Z-scheme pathway. The composite also exhibited a larger specific surface area and retained sufficient magnetic properties for convenient magnetic recovery after photocatalytic reactions. The developed photocatalyst exhibited outstanding multifunctional photocatalytic performance under visible-light irradiation. A hydrogen evolution rate of approximately 1300 μmol h^{-1} g^{-1} was achieved, demonstrating efficient solar-to-hydrogen conversion. During CO_2 photoreduction, CO was identified as the dominant product, whereas CH_4 was produced as a secondary reduction product, indicating effective utilization of photogenerated electrons for carbon conversion. The composite further achieved nearly 98% degradation of model organic pollutants together with an 88% mineralization efficiency, confirming the efficient removal of both dye molecules and their intermediate products. Radical trapping experiments revealed that $\bullet O_2^-$ and •OH radicals were the dominant reactive species, while photogenerated holes also contributed to the oxidation process. Moreover, the photocatalyst retained approximately 94% of its initial activity after five consecutive cycles without noticeable structural or morphological degradation, demonstrating excellent stability and recyclability. The superior photocatalytic activity can be attributed to the synergistic effect of the direct Z-scheme heterojunction. The intimate interfacial contact among $CoFe_2O_4$, $BiVO_4$, Bi_2WO_6, and $g\text{-}C_3N_4$ effectively accelerated charge migration, suppressed electron–hole recombination, expanded visible-light absorption, and preserved strong oxidation and reduction potentials. These collective advantages significantly enhanced hydrogen evolution, CO_2 reduction, and organic pollutant degradation within a single multifunctional photocatalytic platform. The primary novelty of this work lies in the rational design of a quaternary direct Z-scheme photocatalyst capable of simultaneously addressing solar energy conversion, greenhouse gas utilization, and environmental remediation. Unlike conventional binary and ternary

heterojunctions, the present architecture integrates efficient charge separation, broad visible-light harvesting, abundant active sites, and magnetic recoverability within one stable material system. This multifunctional strategy provides an effective approach for overcoming the limitations of rapid charge recombination and insufficient solar-light utilization commonly encountered in conventional photocatalysts.

Key Takeaways

1. A novel $CoFe_2O_4/BiVO_4/Bi_2WO_6/g\text{-}C_3N_4$ direct Z-scheme multi-heterojunction photocatalyst was successfully developed through an in-situ ultrasonication-assisted hydrothermal strategy.
2. The quaternary heterojunction exhibited enhanced visible-light absorption, efficient charge separation, and rapid interfacial charge transfer, leading to superior photocatalytic performance.
3. The composite achieved a hydrogen evolution rate of approximately 1300 μmol h^{-1} g^{-1}, while CO and CH_4 were obtained as the primary products during photocatalytic CO_2 reduction.
4. Nearly 98% degradation of model organic pollutants and 88% mineralization efficiency demonstrated the excellent environmental remediation capability of the developed photocatalyst.
5. The photocatalyst retained approximately 94% of its initial activity after five successive cycles, confirming its excellent stability, magnetic recoverability, and potential for practical solar fuel production and wastewater treatment applications.

REFERENCES

1. H. Kadkhodayan and T. Alizadeh, "Visible-light-driven CO2 photoreduction to solar fuels over a Ni/Cu-loaded Bi2ZnTiO6/g-C3N4 0D/3D/2D QDs Schottky/Z-scheme ternary heterojunction photocatalyst," Jun. 2026. https://doi.org/10.1038/s41598-026-57310-x
2. Iqbal, N., Bano, A., Ahmed, T., M.I. Nabeel, Ullah, J., Musharraf, S. G., & Malik, M. I. (2025). Fish gelatin nanoparticles: An effective carrier for curcumin delivery. Journal of Drug Delivery Science and Technology, 107505. https://doi.org/10.1016/j.jddst.2025.107505.
3. W. Chen, L. Ni, K. Ogino, H. Sun, and J. Bi, "Engineering g-C3N4/Bi2WO6 Composite Photocatalyst for Enhanced Photocatalytic CO2 Reduction," Jan. 2025. https://doi.org/10.3390/coatings15010032
4. J. Chen, Y. Xiao, N. Wang, X. Kang, and D. Wang, "Facile synthesis of a Z-scheme CeO2/C3N4 heterojunction with enhanced charge transfer for CO2 photoreduction," May 2023. https://doi.org/10.1007/s40843-023-2443-0
5. N. Ahmad, S. Rasheed, A. Mohyuddin, B. Fatima, M.I. Nabeel, M.T. Riaz, M. Najam-ul-Haq, D. Hussain, 2D MXenes and their composites; design, synthesis, and environmental sensing applications, Chemosphere 352 (2024) 141280. https://doi.org/https://doi.org/10.1016/j.chemosphere.2024.141280.
6. Ali, M. A., Nabeel, M. I., Hussain, T., Awwad, A., Ismail, E. A., Mustafa, A., & Hassan, N. (2023). Radiation-induced degradation of PVA-26 by UV radiation in the presence of ZnO nanocatalyst. J Biomed Res Environ Sci, 4, 2276.
7. R. Mohamed, H. Abou Oualid, R. Eshaghi Malekshah, B. Ennasraoui, and H. Ighnih, "Efficient photocatalytic removal of ciprofloxacin antibiotic by dual Z-scheme Ag3PO4/g-C3N4/Bi2WO6 under solar irradiation," Jul. 2025. https://doi.org/10.1016/j.jwpe.2025.108394
8. Q. Xie, W. He, S. Liu, C. Li, and J. Zhang, "Bifunctional S-scheme g-C3N4/Bi/BiVO4 hybrid photocatalysts toward artificial carbon cycling," Jan. 2020. https://doi.org/10.1016/S1872-2067(19)63481-9
9. M. Sayed, "Enhancing CO2 photoreduction by construction of g-C3N4/Co-MOFs S-scheme heterojunction," Feb. 2025. https://doi.org/10.1016/j.apsusc.2025.162752
10. Ather, N., Deh-ae, N., Khan, K., Nabeel, M. I., Qasim, M., Joseph, C. G., & Hussain, F. Microplastic Exposure, Oxidative Stress, and Potential Heme Protein Vulnerability in Teleost Fish: Implications for Oxygen Transport and Seafood Quality. Frontiers in Environmental Science, 14, 1904791.
11. M. Sabir, M. Sayed, S. Cao, *et al.,* "Enhancing CO2 photoreduction by construction of g-C3N4/Co-MOFs S-scheme heterojunction," Feb. 2025.
12. H. Kadkhodayan and T. Alizadeh, "Interfacial engineering of Ni/Cu-Loaded A2ZnTiO6/X-doped g-C3N4 schottky-contact Z-scheme heterojunction for enhanced visible-light-driven CO2 photoreduction," Mar. 2026. https://doi.org/10.1007/s10853-026-12582-6
13. M. Ismail, M. Z. H. Makmud, and H. A. Illias, "Multifunctional surface coatings for photovoltaic modules: Anti-soiling, hydrophilic/phobic, and thermal management," IEEE Access, Mar. 2026. https://doi.org/10.1109/ACCESS.2026.3674089
14. M.I. Nabeel, Gulzar, T., Kiran, S., Ahmad, N., Raza, S. A., Batool, U., & Rehan, Z. A. (2025). Tailoring Graphitic Carbon Nitride (g-C3N4) for Multifunctional Applications: Strategies for Overcoming Challenges in Catalysis and Energy Conversion. International Journal of Energy Research, 2025(1), 5599894 https://doi.org/10.1155/er/5599894.
15. M.I. Nabeel, D. Hussain, N. Ahmad, M. Najam-ul-Haq, S.G. Musharraf, Recent advancements in the fabrication and photocatalytic applications of graphitic carbon nitride-tungsten oxide

nanocomposites, Nanoscale Advances 5(19) (2023) 5214-5255. https://doi.org/10.1039/D3NA00159H.
16. J. Zhao, M. Ji, H. Chen, Y.-X. Weng, and J. Zhong, "Interfacial chemical bond modulated Bi19S27Br3/g-C3N4 Z-scheme heterojunction for enhanced photocatalytic CO2 conversion," Feb. 2022. https://doi.org/10.1016/j.apcatb.2022.121162
17. N. T. T. Truc, T.-D. Pham, M. V. Nguyen, D. V. Thuan, and D. Q. Trung, "Advanced NiMoO4/g-C3N4 Z-scheme heterojunction photocatalyst for efficient conversion of CO2 to valuable products," Jun. 2020. https://doi.org/10.1016/j.jallcom.2020.155860
18. L. Guo, Y. You, H. Huang, N. Tian, and T. Ma, "Z-scheme g-C3N4/Bi2O2[BO2(OH)] heterojunction for enhanced photocatalytic CO2 reduction," Feb. 2020. https://doi.org/10.1016/j.jcis.2020.02.025
19. F. W. Ahmad, N. Ahmad, S. Rasheed, M.I. Nabeel, A. Mohyuddin, M.T. Riaz, D. Hussain, Silica-Based Superhydrophobic and Superoleophilic Cotton Fabric with Enhanced Self-Cleaning Properties for Oil-Water Separation and Methylene Blue Degradation, Langmuir 40(11) (2024) 5639-5650. https://doi.org/10.1021/acs.langmuir.3c02821.
20. J. Li, Y. Ma, Y. Xu, P. Li, and J. Guo, "Enhanced photocatalytic degradation activity of Z-scheme heterojunction BiVO4/Cu/g-C3N4 under visible light irradiation," Apr. 2021. https://doi.org/10.1002/wer.1572
21. Ali, T., Ahmad, N., M. I. Nabeel, Xiao, H. M., & Hussain, D. (2024). Facile and Scalable Growth of Bimetallic 3D Ag/MIL125-NH2 on Cotton Fabric for Multifaceted Anti-Wetting and Self-Healing Characteristics, Carbon, 119395. https://doi.org/10.1016/j.carbon.2024.119395.
22. S. Bellamkonda, C. Chakma, S. Guru, B. Neppolian, G. Ranga Rao, *et al.,* "Rational design of plasmonic Ag@CoFe2O4/g-C3N4 p-n heterojunction photocatalysts for efficient overall water splitting," May 2022. https://doi.org/10.1016/j.ijhydene.2022.04.059
23. Ibrahim, M. N. A., Joseph, C. G., Surugau, N., Nabeel, M. I., & Ismail, S. S. (2025). From waste to water cleanup: Preliminary study on sargassum-derived activated carbon (AC) for pollutant adsorption. Mater. Emerg. Technol. Sustain, 1, 2550015.
24. M.I. Nabeel, D. Hussain, N. Ahmad, H.-M. Xiao, S.G. Musharraf, improved visible light-driven photocatalytic degradation of an industrial dye Acid Orange 7 using metal-free sulfur-doped graphitic carbon nitride, Environmental Science: Nano 10(10) (2023) 2810-2830. https://doi.org/10.1039/D3EN00289F.
25. Q. Zhang, M. Liu, S. Liu, L. Qiao, and X. Hu, "Z-scheme g-C3N4/BiVO4 photocatalysts with RGO as electron transport accelerator," Jan. 2020. https://doi.org/10.1007/s10854-019-02573-6
26. M. J. Molaei, "Z-Scheme Heterojunction Photocatalysts: Principles, Engineering Strategies, and Applications in Solar-Driven Energy Conversion and Environmental Remediation," Jul. 2026. https://doi.org/10.1002/jccs.70246
27. M. Lu, Q. Li, C. Zhang, X. Fan, L. Li, *et al.,* "Remarkable photocatalytic activity enhancement of CO2 conversion over 2D/2D g-C3N4/BiVO4 Z-scheme heterojunction promoted by efficient interfacial charge transfer," Apr. 2020. https://doi.org/10.1016/j.carbon.2020.01.038
28. Y. Baghdadi, M. Daboczi, F. Temerov, M. Yang, and J. Cui, "A g-C3N4/rGO/Cs3Bi2Br9 mediated Z-scheme heterojunction for enhanced photocatalytic CO2 reduction," May 2024. https://doi.org/10.1039/D4TA01857E
29. F. A. Qaraah, S. A. Mahyoub, Q. A. Drmosh, A. Qaraah, and F. Xin, "One-step fabrication of unique 3D/2D S, O-doped g-C3N4 S-scheme isotype heterojunction for boosting CO2 photoreduction," Jun. 2023. https://doi.org/10.1016/j.mtsust.2023.100437
30. X. Li, J. Guan, H. Jiang, X. Song, and P. Huo, "rGO modified R-CeO2/g-C3N4 multi-interface contact S-scheme photocatalyst for efficient CO2 photoreduction," Jun. 2021. https://doi.org/10.1016/j.apsusc.2021.150042
31. W.-K. Jo, S. Kumar, S. Eslava, and S. Tonda, "Construction of Bi2WO6/RGO/g-C3N4 2D/2D/2D hybrid Z-scheme heterojunctions with large interfacial contact area for efficient charge separation and high-performance photoreduction of CO2 and H2O into solar fuels," Aug. 2018. https://doi.org/10.1016/j.apcatb.2018.08.056
32. Qasim, M., Manzoor, S., Nabeel, M. I., Hussain, S., Waqas, R., Joseph, C. G., & Suazo-Hernández, J. (2025). Harnessing High-Valent Metals for Catalytic Oxidation: Next-Gen Strategies in Water Remediation and Circular Chemistry. Catalysts, 15(12), 1168 https://doi.org/10.3390/catal15121168.
33. Q. Yao, P. Liu, F. Yang, Y. Zhu, and Y. Pan, "Ferroelectric polarization in Bi0.9Dy0.1FeO3/g-C3N4 Z-scheme heterojunction boosts photocatalytic hydrogen evolution," Aug. 2024. https://doi.org/10.1007/s40843-024-3036-y
34. Q. Wang, Y. Lin, P. Li, M. Ma, and V. Maheskumar, "An efficient Z-scheme (Cr, B) codoped g-C3N4/BiVO4 photocatalyst for water splitting: A hybrid DFT study," Oct. 2020. https://doi.org/10.1016/j.ijhydene.2020.09.252
35. M.I. Nabeel, Hussain, D., Ahmad, N., Xiao, H. M., Ahmad, W., & Musharraf, S. G. (2025). Facile one-pot synthesis of metal and non-metal doped g-C3N4 photocatalyst for rapid acetaminophen remediation. Carbon, 120472.https://doi.org/10.1016/j.carbon.2025.120472.
36. Kiran, S., Gulzar, T., Ijaz, M. U., Sethi, A., Nadeem, L., Yousaf, A., ... & Nabeel, M. I. (2026). Sonochemical technology in the degradation of textile dye effluents. In Sonochemistry for Textile

and Fibre Engineering (pp. 193-215). Woodhead Publishing.
37. R. Song, S. Kang, L. Yao, L. Zheng, and D. Yu, "Construction of an La-BiVO4/O-Doped g-C3N4 Heterojunction Photocatalyst Embedded in Electrospinning Nanofibers," May 2023. https://doi.org/10.1021/acs.langmuir.2c03356
38. L. Pei, Z. Luo, X. Wang, Z. Ma, and Y. Nie, *et al.,* "Tunable CO2-to-Syngas Conversion via Strong Electronic Coupling in S-scheme ZnGa2O4/g-C3N4 Photocatalysts," Jul. 2023. https://doi.org/10.1016/j.jcis.2023.07.148
39. M.I. Nabeel, Ahmad, N., Arif, S., Hussain, D., & Musharraf, S. G. (2025). Facile Two-Step Synthesis of Yttrium-Doped g-C3N4 for Enhanced Photocatalytic Degradation of Methylene Blue with Self-Cleaning Properties. Nanoscale Advances. https://doi.org/10.1039/D5NA00600G.
40. Ullah, Z., Joseph, C. G., Tian, Z. Y., Yasin, M., Khan, M. N., Ali, S., ... & M. I. Nabeel, (2025). The Production of Biochar and Its Impact on the Removal of Various Emerging Pollutants from Wastewater: A Review. Toxics, 13(12), 1079 https://doi.org/10.3390/toxics13121079.
41. T. Liu, Y. Wu, H. Wang, J. Lu, and Y. Luo, "Defect-Engineered Z-Scheme Heterojunction of Fe-MOFs/Bi2WO6 for Solar-Driven CO2 Conversion: Synergistic Surface Catalysis and Interfacial Charge Dynamics," Apr. 2025. https://doi.org/10.3390/nano15080618
42. X. Zhang, K. Matras-Postolek, P. Yang, and S. P. Jiang, *et al.,* "Z-Scheme WOx/Cu-g-C3N4 Heterojunction Nanoarchitectonics with Promoted Charge Separation and Transfer towards Efficient Full Solar-Spectrum Photocatalysis," Jan. 2023. https://doi.org/10.1016/j.jcis.2023.01.052
43. Y. Xu, J. Yu, J. Long, L. Tu, and W. Dai, *et al.,* "Z-Scheme Heterojunction of SnS2/Bi2WO6 for Photoreduction of CO2 to 100% Alcohol Products by Promoting the Separation of Photogenerated Charges," Jun. 2022. https://doi.org/10.3390/nano12122030
44. X. Yin, X. Sun, D. Li, W. Xie, and Y. Mao, *et al.,* "2D/2D Phosphorus-Doped g-C3N4/Bi2WO6 Direct Z-Scheme Heterojunction Photocatalytic System for Tetracycline Hydrochloride (TC-HCl) Degradation," Nov. 2022. https://doi.org/10.3390/ijerph192214935
45. Shahzad, F., Hussain, E., Nadeem, N., Nabeel, M. I., Saeed, M., Joseph, C. G., ... & Sajid, M. (2026). GREEN SYNTHESIS OF COPPER OXIDE NANOPARTICLES TO HARVEST THE LIGHT FOR PHOTOCATALYTIC DEGRADATION OF DYES METHYLENE BLUE AND METHYL ORANGE. Borneo Science| The Journal of Science and Technology, 47(1). https://doi.org/10.51200/bsj.v47i1.7565
46. Gulzar, T., Ullah, H., Maqsood, A., Abrar, S., Nabeel, M. I., Kanwal, A., & Raza, S. A. (2025). Panoramic View of Biomedical Textiles and Their Synthetic Strategies. In Biomedical Textiles (pp. 1-34). Jenny Stanford Publishing.
47. J. Qin, M. Zhao, Y. Zhang, J. Shen, and X. Wang, "Probing Local Structure and Electronic Structure of A-Fe2o3/G-C3n4 S-Scheme Heterojunctions for Boosting Co2 Photoreduction," Jan. 2024. https://doi.org/10.2139/ssrn.4909247
48. Y. Zhang, N. Nwaji, L. Wu, M. Jin, and J. Lee, *et al.,* "MAPbBr3/Bi2WO6 Z-scheme-heterojunction photocatalysts for photocatalytic CO2 reduction," Jan. 2024. https://doi.org/10.1007/s10853-023-09220-w
49. M.I.Nabeel, D.Hussain, S.G. Musharraf, N. Ahmad, Advanced Doped and Composite Graphitic Carbon Nitride Photocatalysts for Efficient Degradation of Organic Pollutants under Visible Light, in Proceedings of The 1st International Online Conference on Xenobiotics, 22 June–23 June 2026, MDPI: Basel, Switzerland
50. R. LaChance, B. Adeli, and F. Taghipour, "Solar Fuel Generation by 2D Self-Assembled g-C3N4/BiVO4 Z-Scheme," Dec. 2023. https://doi.org/10.1002/solr.202300677
51. H. Xie, Y. Zhao, H. Li, Y. Xu, and X. Chen, "2D BiVO4/g-C3N4 Z-scheme photocatalyst for enhanced overall water splitting," Aug. 2019. https://doi.org/10.1007/s10853-019-03664-9
52. K. Wu, S. Song, H. Wu, J. Guo, L. Zhang, *et al.,* "Facile synthesis of Bi2WO6/C3N4/Ti3C2 composite as Z-scheme photocatalyst for efficient ciprofloxacin degradation and H2 production," Nov. 2020. https://doi.org/10.1016/j.apcata.2020.117869
53. M.I. Nabeel., Hussain, D., Ahmad, N., Saeed, A., Ali, K., Xiao, H. M., & Musharraf, S. G. (2025). Facile Synthesis of Robust 2D Z-scheme Ultrathin Sulfur Doped g-C3N4-Tungsten Oxide Composite by High Pressure Vacuum Filtration for 5-FU Detoxification. Surfaces and Interfaces, 108278.https://doi.org/10.1016/j.surfin.2025.108278.
54. C. Zhang, R. Li, Y. Zhao, and M. Wang, "Construction of Z-Scheme Bi2WO6/g-C3N4 Heterojunction Photocatalysts with Enhanced Visible-Light Photocatalytic Activity," Apr. 2017. https://doi.org/10.1071/CH16507
55. P. Mane, H. Bae, V. Burungale, S.-W. Lee, and M. Misra, "Interface-engineered Z-scheme of BiVO4/g-C3N4 photoanode for boosted photoelectrochemical water splitting and organic contaminant elimination under solar light," Aug. 2022. https://doi.org/10.1016/j.chemosphere.2022.136166
56. Arif, S., Rasheed, S., Ahmad, N., M. I. Nabeel, Ahmad, W., Alomayri, T., ... & Musharraf, S. G. (2026). Carbon-based materials for photocatalytic degradation of pharmaceuticals and drugs. Journal of Water Process Engineering, 81, 109274 https://doi.org/10.1016/j.jwpe.2025.109274.
57. Y. Feng, D. Chen, Y. Zhong, Z. He, and S. Ma, *et al.,* "A Lead-Free 0D/2D Cs3Bi2Br9/Bi2WO6 S-

Scheme Heterojunction for Efficient Photoreduction of CO2," Feb. 2023. https://doi.org/10.1021/acsami.2c19703
58. M. Sabir, M. Sayed, I. Riaz, G. Qiu, and M. Tahir, "Ni-MOF/g-C3N4 S-Scheme Heterojunction for Efficient Photocatalytic CO2 Reduction," Jul. 2025. https://doi.org/10.3390/ma18143419
59. Z. Wei, F. Yue, H. Haibao, Z. Pengcheng, and L. Jing, "A novel Z-scheme Ag3VO4/BiVO4 heterojunction photocatalyst: Study on the excellent photocatalytic performance and photocatalytic mechanism," May 2019. https://doi.org/10.1016/j.apcatb.2019.01.001
60. Raza, H. Shen, A. A. Haidry, *et al.,* "Novel Cu2ZnSnS4/Pt/g-C3N4 heterojunction photocatalyst with straddling band configuration for enhanced solar to fuel conversion," Nov. 2020. https://doi.org/10.1016/j.apcatb.2020.119239
61. Y. Peng, P.-Y. Dugas, K. C. Szeto, C. C. Santini, S. Daniele, *et al.,* "Interplay Between Ionic Liquids, Kolbe Chemistry, and 2D Photocatalyst Supports in Aqueous CO2 Photoreduction over Pd/TiO2 and Pd/g-C3N4," Dec. 2025. https://doi.org/10.3390/catal15121128
62. G. Rana, R. Verma, E. A. Alabdullkarem, S. K. Rao, and K.-Y. A. Lin, "Z-Scheme CoFe2O4/g-C3N4/MWCNT catalyst for the degradation of organic pollutants: electrochemical evaluation and HPLC analysis of the intermediates," Jun. 2026. https://doi.org/10.1039/d6ra02055k
63. R. Zhang and K. Zeng, "A novel flower-like dual Z-scheme BiSI/Bi2WO6/g-C3N4 photocatalyst has excellent photocatalytic activity for the degradation of organic pollutants under visible light," Mar. 2021. https://doi.org/10.1016/j.diamond.2021.108343
64. Z. Zhai, J. Bi, L. Wang, N. Liu, Y. Wang, *et al.,* "Synergistic Photocatalytic Removal of U(VI) and Tetracycline over a Dual Z-scheme g-C3N4/Bi2MoO6/Bi2WO6 Heterojunction," Jan. 2026. https://doi.org/10.2139/ssrn.6777198
65. Z. Zhang, D. Zhang, L. Lyu, G. Cui, and H. Lu, "In Situ Formation of Z-Scheme Bi2WO6/WO3 Heterojunctions for Gas-Phase CO2 Photoreduction with H2O by Photohydrothermal Treatment," Oct. 2022. https://doi.org/10.3390/catal12101237
66. R. Sun, Q. Shi, M. Zhang, L. Xie, and J. Chen, "Enhanced photocatalytic oxidation of toluene with a coral-like direct Z-scheme BiVO4/g-C3N4 photocatalyst," Apr. 2017. https://doi.org/10.1016/j.jallcom.2017.04.108
67. P. Zhu, S. Zhang, R. Liu, D. Luo, and H. Yao, "Investigation of an enhanced Z-scheme magnetic recyclable BiVO4/GO/CoFe2O4 photocatalyst with visible-light-driven for highly efficient degradation of antibiotics," Jul. 2022. https://doi.org/10.1016/j.jssc.2022.123379
68. Y. Baghdadi, F. Temerov, J. Cui, M. Daboczi, and E. Rattner, "Cs3Bi2Br9/g-C3N4 Direct Z-Scheme Heterojunction for Enhanced Photocatalytic Reduction of CO2 to CO," Oct. 2023. https://doi.org/10.1021/acs.chemmater.3c01635
69. P. Sang and J. H. Kim, "Role of g-C3N4 in Fabrication of BiVO4/WO3 Z-scheme Heterojunction for high Photoelectrochemical Performances with Enhanced Light Harvesting," Oct. 2022. https://doi.org/10.1007/s40684-022-00478-0
70. Z. Zhao, J. Bian, L. Zhao, H. Wu, and S. Xu, "Construction of 2D Zn-MOF/BiVO4 S-scheme heterojunction for efficient photocatalytic CO2 conversion under visible light irradiation," May 2022. https://doi.org/10.1016/S1872-2067(21)64005-6
71. P. Sang and J. H. Kim, "Role of g-C3N4 in Fabrication of BiVO4/WO3 Z-scheme Heterojunction for high Photoelectrochemical Performances with Enhanced Light Harvesting," Oct. 2022. https://doi.org/10.1007/s40684-022-00478-0
72. J. Ren, Q. Ma, X. Sun, S.-F. Wang, and G. Liu, "Interface-engineering enhanced photocatalytic conversion of CO2 into solar fuels over S-type Co-Bi2WO6@Ce-MOF heterostructured photocatalysts," Mar. 2025. https://doi.org/10.1016/j.jcis.2025.137452
73. Z. Wang, R. Liu, J. Zhang, and K. Dai, "S-scheme Porous g-C3N4/Ag2MoO4 Heterojunction Composite for CO2 Photoreduction," Jun. 2022. https://doi.org/10.14102/j.cnki.0254-5861.2022-0108
74. W. Ali, F. Ali, W. Muhammad, M. Z. Ansar, and Z. U. Khan, "Construction of 2D/2D α-Fe2O3/g-C3N4 Z-scheme photocatalysts with SnO2 as an energy platform for directed charge transfer in cascade heterojunction: Photocatalytic CO2 reduction and pollutant degradation," Mar. 2025. https://doi.org/10.1016/j.jcis.2025.137459
75. D. Kim and K. Yong, "Boron doping induced charge transfer switching of a C3N4/ZnO photocatalyst from Z-scheme to type II to enhance photocatalytic hydrogen production," Mar. 2021. https://doi.org/10.1016/j.apcatb.2020.119538
76. L. Jiang, H. Du, L. Li, X. Guan, and Y. Zhang, "Sequential Growth of Cs3Bi2I9/BiVO4 Direct Z-Scheme Heterojunction for Visible-Light-Driven Photocatalytic CO2 Reduction," Dec. 2023. https://doi.org/10.1007/s12209-023-00376-9
77. B. Ma, Y. Zha, P. Yu, G. Chen, and Y. Guo, "Hydrothermal nanoarchitectonics of Z-scheme g-C3N4/Bi2WO6 heterojunction with enhanced adsorption and photocatalytic activity for fluoroquinolone antibiotics removal: Kinetics, mechanism and degradation pathway," Apr. 2023. https://doi.org/10.1016/j.jallcom.2023.170061
78. Y. Li, Z. Xia, Q. Yang, L. Wang, Y. Xing, *et al.,* "Review on g-C3N4-based S-scheme Heterojunction Photocatalysts," Apr. 2022. https://doi.org/10.1016/j.jmst.2022.02.035

79. S. Tang, Y. Ma, H. Wang, Y. Liang, and X. Xu, "One-Pot Synthesis of 2D-2D WO3/g-C3N4 Photocatalyst in Reverse Microemulsion System via Supercritical CO2 for Enhanced Hydrogen Generation," Apr. 2023. https://doi.org/10.1002/cssc.202202184
80. P. Zhu, D. Luo, M. Liu, M. Duan, J. Lin, *et al.,* "Flower-globular BiOI/BiVO4/g-C3N4 with a dual Z-scheme heterojunction for highly efficient degradation of antibiotics under visible light," Jun. 2022. https://doi.org/10.1016/j.seppur.2022.121503
81. Q. Chen, J. Huang, D. Chu, L. Cao, and X. Li, "Accelerated Photogenerated Charge Separation Driven Synergistically by the Interfacial Electric Field and Work Function in Z-Scheme Zn-Ni2P/G-C3N4 for Efficient Photocatalytic Hydrogen Evolution," Aug. 2025. https://doi.org/10.1002/EXP.20240189
82. Z. Duan, X. Zhao, L. Chen, *et al.,* "BiVO4/Cu0.4V2O5 composites as a novel Z-scheme photocatalyst for visible-light-driven CO2 conversion," Oct. 2020. https://doi.org/10.1016/j.jece.2020.104628
83. Y. Bai, Z. Chen, D. Gu, R. Wang, and J. He, "Modification of AgInS2/g-C3N4 Z-Scheme Heterojunction by Ag Nanoparticles to Increase Photocatalytic Rate," Apr. 2025. https://doi.org/10.1007/s10562-025-04975-0
84. C. Yang, Q. Zhang, W. Wang, B. Cheng, and J. Yu, "2D/2D g-C3N4@BiOI S-scheme heterojunction with gas-liquid-solid triphase interface for highly efficient CO2 photoreduction," Apr. 2024. https://doi.org/10.1007/s40843-024-2789-0
85. L. Gaozong, S. Xie, H. Peng, H. Huang, H. Ning, *et al.,* "Study on Photocatalytic Oxidation of MG and reduction of Cr (VI) by Sulfur-doped g-C3N4/Bi2WO6 tungstate Z-type heterojunction under LED Light source irradiation," Jan. 2026. https://doi.org/10.2139/ssrn.6439371
86. G. Gebreslassie, M. Gebrezgiabher, B. Lin, M. Thomas, and W. Linert, *et al.,* "Direct Z-Scheme CoFe2O4-Loaded g-C3N4 Photocatalyst with High Degradation Efficiency of Methylene Blue under Visible-Light Irradiation," Mar. 2023. https://doi.org/10.3390/inorganics11030119
87. M. H. Aziz, M. Asif, M. Fatima, M. T. Khan, and A. F. El-kott, *et al.,* "Synergistic impact of CoFe2O4/g-C3N4/WO3 as dual Z-scheme photocatalyst for improving tetracycline (TC-HCl) degradation and antibacterial performance," Apr. 2026. https://doi.org/10.1007/s10853-026-12645-8
88. M. Sayed, B. Zhu, P. Kuang, X. Liu, and B. Cheng, *et al.,* "EPR Investigation on Electron Transfer of 2D/3D g-C3N4/ZnO S-Scheme Heterojunction for Enhanced CO2 Photoreduction," Oct. 2021. https://doi.org/10.1002/adsu.202100264
89. H. Ren, X. Sun, T. Li, Z. Ren, and C. Song, "Preparation of a Z-scheme BiVO4/Cu2O/PPy heterojunction and studying its CO2 reducing properties," Apr. 2025. https://doi.org/10.1039/d4ra08130g
90. J. Jia, Q. Zhang, K. Li, Y. Zhang, and E. Liu, "Recent advances on g–C3N4–based Z-scheme photocatalysts: Structural design and photocatalytic applications," Oct. 2022. https://doi.org/10.1016/j.ijhydene.2022.09.272
91. N. Madima, K. K. Kefeni, A. T. Kuvarega, S. B. Mishra, and A. K. Mishra, *et al.,* "Visible-light-driven Z-scheme ternary Fe3O4/TiO2/g-C3N4 nanocomposite as reusable photocatalyst for efficient removal of dyes and chromium in water," Dec. 2022. https://doi.org/10.1016/j.matchemphys.2022.127233
92. I.-H. Tsai, C.-H. Fu, T.-H. Lin, S.-Y. Lin, and E. W.-G. Diau, "Enhanced Photocatalytic Performance for CO2 Reduction Using an Indirect Z-Scheme Heterojunction Photocatalyst," May 2026. https://doi.org/10.1002/cssc.70716
93. J. Wu, K. Li, S. Yang, C. Song, and X. Guo, "In-situ construction of BiOBr/Bi2WO6 S-scheme heterojunction nanoflowers for highly efficient CO2 photoreduction: Regulation of morphology and surface oxygen vacancy," Sep. 2022. https://doi.org/10.1016/j.cej.2022.139493
94. M. Osemba, "Vacancy-Regulated Dual Single-Atom COF/g-C3N4 S-Scheme Heterostructures for Selective Multi-Carbon Product Formation via Solar-Driven Artificial Photosynthesis," Jul. 2026. https://doi.org/10.26434/chemrxiv.15005969/v1
95. C. Luo, Q. Long, B. Cheng, B. Zhu, and L. Wang, "A DFT Study on S-Scheme Heterojunction Consisting of Pt Single Atom Loaded G-C3N4 and BiOCl for Photocatalytic CO2 Reduction," Jun. 2023. https://doi.org/10.3866/PKU.WHXB202212026
96. Z. Tang, C. Wang, W. He, Y. Wei, and Z. Zhao, "The Z-scheme g-C3N4/3DOM-WO3 photocatalysts with enhanced activity for CO2 photoreduction into CO," Jul. 2021. https://doi.org/10.1016/j.cclet.2021.07.020
97. J. Geng, S. Guo, Z. Zou, Z. Yuan, and D. Zhang, "0D/2D CeO2/BiVO4 S-scheme photocatalyst for production of solar fuels from CO2," Feb. 2023. https://doi.org/10.1016/j.fuel.2022.126417
98. G. Wang, Z. Luo, Q. Wei, C. Peng, and Q. Liu, "Dual-metal sites CuInS2/g-C3N4 Z-scheme heterojunction with efficient photocatalytic CO2 reduction selectivity," Dec. 2022. https://doi.org/10.1016/j.fuproc.2022.107530
99. Y. Yang, J. Wu, T. Xiao, Z. Tang, and J. Shen, "Urchin-like hierarchical CoZnAl-LDH/RGO/g-C3N4 hybrid as a Z-scheme photocatalyst for efficient and selective CO2 reduction," May 2019. https://doi.org/10.1016/j.apcatb.2019.117771
100. B. Palanivel, M. Lallimathi, B. Arjunkumar, M. Shkir, and T. Alshahrani, *et al.,* "rGO supported g-C3N4 /CoFe2O4 heterojunction: Visible-light-active photocatalyst for effective utilization of

H2O2 to organic pollutant degradation and OH• radicals production," Nov. 2020. https://doi.org/10.1016/j.jece.2020.104698
101. M. Dong, S. Yang, P. Zhou, Z. Huang, and S. Tu, *et al.,* "UiO-66-mediated Bi2WO6/AgI heterojunction photocatalyst for efficient visible-light-driven tetracycline degradation," Jul. 2026. https://doi.org/10.1007/s10853-026-13211-y
102. Z. Zhu, C. Ma, K. Yu, Z. Lu, and Z. Liu, "Fabrication of CoFe2O4-modified and HNTs-supported g-C3N4 heterojunction photocatalysts for enhancing MBT degradation activity under visible light," Apr. 2020. https://doi.org/10.1007/s10853-019-04170-8
103. S. Tahir, Z. A. Rehan, M. S. Khan, G. Mustafa, and S. Noreen, "Design, synthesis and characterization of g-C3N4/GO/CoFe2O4 nanocomposite for efficient photocatalytic degradation of pollutants using sunlight," May 2026. https://doi.org/10.1007/s13762-026-07252-8
104. Q. Li, L. Li, X. Long, Y. Tu, and L. Ling, "Rational design of MIL-88A(Fe)/Bi2WO6 heterojunctions as an efficient photocatalyst for organic pollutant degradation under visible light irradiation," Aug. 2021. https://doi.org/10.1016/j.optmat.2021.111260
105. Gulzar, T., Sethi, A., Maqsood, A., Batool, U., Maqsood, N., Raza, S. A., & Nabeel, M. I. (2025). Developmental Vistas for Bioactive Textile Engineering. In Biomedical Textiles (pp. 133-166). Jenny Stanford Publishing.
106. O. T. K. Nguyen, T. V. Huynh, B. G. Tran, H. Q. Ha, V. H. Nguyen, and Q.-M. T. Doan, "Synthesis of BiVO4/g-C3N4 heterojunction photocatalyst for enhanced doxycycline degradation under LED light illumination," Jan. 2026. https://doi.org/10.1016/j.mseb.2025.118804
107. G. Abimannan, "BiVO4/g-C3N4 as an efficient photocatalyst for degradation of organic pollutants," Conference Paper, Mar. 2023.
108. J. Li, Y. Ma, Y. Xu, P. Li, and J. Guo, "Enhanced photocatalytic degradation activity of Z-scheme heterojunction BiVO4/Cu/g-C3N4 under visible light irradiation," Apr. 2021. https://doi.org/10.1002/wer.1572
109. T. H. T. Vu, N. Q. T. Ton, and T. G. B. Nguyen, "Construction of SrTiO3/g-C3N4 Heterojunction for Improved Visible-Light-Driven Photocatalytic Activity toward Decomposition of Organic Pollutants in Water," Sep. 2025. https://doi.org/10.32508/stdj.v28i3.4465
110. J. Zhao, J. Yan, H. Jia, S. Zhong, and X. Zhang, *et al.,* "BiVO4/g-C3N4 composite visible-light photocatalyst for effective elimination of aqueous organic pollutants," Aug. 2016. https://doi.org/10.1016/j.molcata.2016.08.025
111. B. Rabeie, N. M. Mahmoodi, and H. Kazemian, "Visible light assisted magnetic COF/HKUST/CoFe2O4 composite as a novel photocatalyst: green synthesis and efficient degradation of pollutants (dye and pharmaceutical) in water," Mar. 2026. https://doi.org/10.1007/s42114-026-01696-9
112. M. Nanjappan, H. Rajagopalan, V. Pandurangan, and P. Elaiyaraja, "Structural, optical and magnetic properties of CoFe2O4 coupled with Sulfur-doped g-C3N4 for enhanced visible light-driven photocatalytic antibacterial drug and industrial dye degradation applications," May 2026. https://doi.org/10.1007/s42247-026-01425-4
113. X. Liu, Y. Fang, C. Yang, G. I. Abdulrasheed, and X. Feng, "Oxygen Vacancy-Engineered pg-C3N4/CdS/BiOCl Ternary Heterojunction Photocatalysts for Enhanced Visible-Light-Driven Degradation of Tetracycline," Jan. 2026. https://doi.org/10.2139/ssrn.6517200
114. R. Zhang and K. Zeng, "A novel flower-like dual Z-scheme BiSI/Bi2WO6/g-C3N4 photocatalyst has excellent photocatalytic activity for the degradation of organic pollutants under visible light," Mar. 2021. https://doi.org/10.1016/j.diamond.2021.108343
115. M. Alhaddad and M. S. Amin, "Removal of ciprofloxacin applying Pt@BiVO4-g-C3N4 nanocomposite under visible light," Feb. 2022. https://doi.org/10.1016/j.optmat.2022.111976
116. G. Rana, R. Verma, E. A. Alabdullkarem, S. K. Rao, and K.-Y. A. Lin, "Z-Scheme CoFe2O4/g-C3N4/MWCNT catalyst for the degradation of organic pollutants: electrochemical evaluation and HPLC analysis of the intermediates," Jun. 2026. https://doi.org/10.1039/d6ra02055k
117. Y. Tang, X. Cheng, J. Wang, M. Gao, and X. Deng, "Construction of g-C3N4/NCQDs/FeTiO3 heterojunction and its visible light-driven degradation performance study on methylene blue," Jun. 2025. https://doi.org/10.1007/s10854-025-15060-y
118. R. Kumari and R. Kumar, "Enhanced photocatalytic performance of 2D/3D g-C3N4/MoS2 heterojunction for water remediation of real-world pollutants," Jul. 2025. https://doi.org/10.1063/5.0266899
119. P. Zhu, S. Zhang, R. Liu, D. Luo, and H. Yao, "Investigation of an enhanced Z-scheme magnetic recyclable BiVO4/GO/CoFe2O4 photocatalyst with visible-light-driven for highly efficient degradation of antibiotics," Jul. 2022. https://doi.org/10.1016/j.jssc.2022.123379
120. M. Zhang, T. Wang, C. Bian, N. Yang, and H. Qi, *et al.,* "Designing novel step-scheme heterojunction g-C3N4/TMCs/GO with effective charge transfer for photocatalytic degradation of organic pollutant under visible light," Nov. 2022. https://doi.org/10.1016/j.seppur.2022.122736
121. S. Jiang, G. Zheng, F. Zhang, H. Yu, and Y. Cai, *et al.,* "CTAB-regulated Bi/Bi2WO6 heterojunction with effectively enhanced visible light photocatalytic degradation of pollutants," May 2026. https://doi.org/10.1007/s10854-026-17487-3
122. K. Wang, X. Su, Z. Zhou, L. Hu, and H. Li, *et al.,* "Dual-Effect of S-Scheme Heterojunction and

CQDs Strengthens the Charge Separation and Transfer in CQDs-g-C3N4/TiO2 Photocatalysts Toward Efficient Tetracycline Degradation," Jan. 2026. https://doi.org/10.3390/nano16030181

123. K. Milošević, D. Lončarević, T. Mudrinić, M. Kalagasidis Krušić, and J. Dostanić, *et al.,* "Mechanistic insights into the simultaneous visible-light induced photodegradation of organic pollutants by g-C3N4/titanate heterojunction," Jan. 2023. https://doi.org/10.1007/s11051-023-05673-x
124. Chowdhury, S. Balu, K.-W. Lan, L. W.-C. Lee, and T. C.-K. Yang, "Synergistic Effect of BiVO4/P-g-C3N4 Heterojunction with Enhanced Optoelectronic Properties on Synthetic Colorants under Visible Light," Jun. 2023. https://doi.org/10.3390/colorants2020019
125. X. Zheng, X. Zhang, Y. Cai, S. Zhao, and S. Wang, "Efficient degradation of bisphenol A with MoS2/BiVO4 hetero-nanoflower as a heterogenous peroxymonosulfate activator under visible-light irradiation," Dec. 2021. https://doi.org/10.1016/j.chemosphere.2021.133158
126. M. Ismael and M. Wark, "Photocatalytic activity of CoFe2O4/g-C3N4 nanocomposite toward degradation of different organic pollutants and their inactivity toward hydrogen production: The role of the conduction band position," Jan. 2022. https://doi.org/10.1016/j.flatc.2022.100337
127. V. Rathi, A. Panneerselvam, and R. Sathiyapriya, *et al.,* "A novel hydrothermal induced BiVO4/g-C3N4 heterojunctions visible-light photocatalyst for effective elimination of aqueous organic pollutants," Jul. 2020. https://doi.org/10.1016/j.vacuum.2020.109458
128. P. Mohan, S. Mallapur, C. P. Prathibha, B. M. Rajesh, and S. Kandaiah, "Integrating the bicrystalline monoclinic-tetragonal BiVO4 with g-C3N4 to form S-scheme heterojunction for bromocresol green dye degradation under visible light," Jan. 2026. https://doi.org/10.1007/s10854-025-16555-4
129. Y. Qin, H. Li, J. Lu, Y. Ding, and C. Ma, "Fabrication of Bi2WO6/In2O3 photocatalysts with efficient photocatalytic performance for the degradation of organic pollutants: Insight into the role of oxygen vacancy and heterojunction," May 2020. https://doi.org/10.1016/j.apt.2020.05.014
130. K. Perumal, P. Krishnan, B. R., K. Anandan, and A. C., "Dual Z-Scheme g-C3N4/MoS2/ZnO Photocatalyst for Efficient Visible-Light Antibiotic Degradation," Jun. 2026. https://doi.org/10.1007/s42250-026-01738-1
131. X. Li, T. Chen, Y. Qiu, Z. Zhu, and H. Zhang, "Magnetic dual Z-scheme g-C3N4/BiVO4/CuFe2O4 heterojunction as an efficient visible-light-driven peroxymonosulfate activator for levofloxacin degradation," Oct. 2022. https://doi.org/10.1016/j.cej.2022.139659
132. K. Shekhawat, V. K. Mishra, S. Pooniya, A. Bagaria, and D. Bhalothia, "Rapid visible-light-driven Rose Bengal dye degradation over a hydrothermally assembled g-C3N4-MXene composite," Jun. 2026. https://doi.org/10.1007/s42452-026-08945-y
133. P. Zhu, D. Luo, M. Liu, M. Duan, and J. Lin, "Flower-globular BiOI/BiVO4/g-C3N4 with a dual Z-scheme heterojunction for highly efficient degradation of antibiotics under visible light," Jun. 2022. https://doi.org/10.1016/j.seppur.2022.121503
134. T.-Y. Huang, P. Naruphontjirakul, J.-Y. Lin, and W.-T. Su, "Enhanced Visible-Light-Driven Degradation of Benzophenone-3 over g-C3N4/WO3 Z-Scheme Heterojunction Nanocomposites," Jan. 2026. https://doi.org/10.2139/ssrn.6845403
135. H. H. Haitosa, O. A. Zelekew, Y.-N. Wu, and D. M. Kabtamu, "Synergistic Mg Doping and Phase Engineering of MoS2/g-C3N4 Catalysts: Boosting Visible-Light-Driven Photo-Fenton Pollutant Remediation," Oct. 2025.
136. Sharma, S. K. Kanth, S. Xu, N. Han, and Z. Lei, "Visible light driven g-C3N4/Bi4NbO8X (X=Cl, Br) heterojunction photocatalyst for the degradation of organic pollutants," Nov. 2021. https://doi.org/10.1016/j.jallcom.2021.162576
137. X. Zhang, Y. Gong, X. Dong, X. Zhang, and C. Ma, "Fabrication and efficient visible light-induced photocatalytic activity of Bi2WO6/BiVO4 heterojunction," Oct. 2012. https://doi.org/10.1016/j.matchemphys.2012.07.013
138. G. Zhao, J. Ding, F. Zhou, X. Chen, L. Wei, *et al.,* "Construction of a visible-light-driven magnetic dual Z-scheme BiVO4/g-C3N4/NiFe2O4 photocatalyst for effective removal of ofloxacin: Mechanisms and degradation pathway," Aug. 2020. https://doi.org/10.1016/j.cej.2020.126704
139. Y. Xu, B. Hu, J. Liu, K. Tao, and R. Wang, "Visible light-activated degradation of microcystin-LR by ultrathin g-C3N4 nanosheets-based heterojunction photocatalyst," Sep. 2019. https://doi.org/10.1111/jace.16773
140. Maosheng Tian, Chenyan Hu, Junxia Yu, and Lianguo Chen, "Carbon quantum dots (CQDs) mediated Z-scheme g–C3N4–CQDs/BiVO4 heterojunction with enhanced visible light photocatalytic degradation of Paraben," Mar. 2023. https://doi.org/10.1016/j.chemosphere.2023.138248
141. Dang Van Do, Cham Thanh Le, Xoan Thi Nguyen, Son Thanh Le, and Khai Manh Nguyen, "Photodegradation of diclofenac in aqueous media via a HO˙ radical pathway using CeO2/g-C3N4 heterojunction under visible light: experimental and computational insights," Oct. 2025. https://doi.org/10.1039/D5RA06295K
142. Naveed Ahmad, Chung Feng Jaffrey Kuo, and Mujahid Mustaqeem, "Synthesis of novel CuNb2O6/g-C3N4 binary photocatalyst towards efficient visible light reduction of Cr (VI) and dyes degradation for environmental remediation," Mar.

2022. https://doi.org/10.1016/j.chemosphere.2022.134153
143. Yun-hui Si, Wei-min Chen, Shao-ke Shang, Yu Xia, and Xie-rong Zeng, "g-C3N4/Pt/BiVO4 nanocomposites for highly efficient visible-light photocatalytic removal of contaminants and hydrogen generation," Jan. 2020. https://doi.org/10.1088/1361-6528/ab5bc5
144. N. Ahmad, M.I. Nabeel, S.J. Ali, B. Fatima, H.N. Rashid, M. Najam-ul-Haq, S.G. Musharraf, D. Hussain, hierarchically grown CeO2/GO on nylon filter with enhanced hydrophilicity and permeation flux for oil-water separation, Sustainable Materials and Technologies 37 (2023) e00698. https://doi.org/https://doi.org/10.1016/j.susmat.2023.e00698.
145. Mazen R. Alrahili, Mohamed Abdel Rafea, Magdi E. A. Zaki, M. Khairy, and Mohamed R. El-Aassar, "Rationally designed In–CeO2/g-C3N4 S-scheme heterojunction photocatalyst with tuned redox ability for the photocatalytic degradation of pharmaceutical contaminants," Dec. 2025. https://doi.org/10.1039/D5RA07023F
146. Garima Rana, Pooja Dhiman, Amit Kumar, Elmuez A. Dawi, and Gaurav Sharma, "Visible-Light Driven Z-scheme g-C3N4/Fe-MOF Photocatalyst for Degradation of Organic Pollutants," Feb. 2024. https://doi.org/10.1007/s10904-024-03005-7
147. Qasim, M., Manzoor, S., M. I. Nabeel, Ullah, Q., Sair, Y.Z., Khomphet, T., Joseph, C.G., Raza, A., Suazo-Hernández, J. and Gulzar, T., 2026. Waste-Derived Nanocomposites as Dual-Function Materials for Water and Energy Sustainability. Frontiers in Sustainability, 7, p.1777462.(2026) http://doi.org/10.3389/frsus.2026.1777462.
148. N.M. Khan, A. Moied, S. Kiran, T. Gulzar, I. Pervez, R. Shahid, M. I. Nabeel, A. Ali, Prunus armeniaca assisted green synthesis of Fe2O3 /NiO nanohybrids using unripend fruit extract for remediation of Acid Orange 7 Dye. A Sustainable Environmental Cleaner Approach. Waste and Biomass Valorization, 2024. https://doi.org/10.1007/s12649-024-02738-3.
149. Xiaodan Miao, Xiaowen Liu, Yuanfan Wang, and Pei Chen, "Enhanced photocatalytic degradation properties of a g-C3N4/BiVO4 heterostructure system induced by surface and interface heterojunctions," Mar. 2024. https://doi.org/10.1007/s10853-024-09548-x
150. Qin Lisiyuan he, Liang Wang, Mengxin Zhao, and Tao Guo, "A novel Z-scheme heterojunction g-C3N4/g-C3N4/Pr6O11 for efficient visible-light photocatalytic degradation of sulfonamide," Feb. 2024. https://doi.org/10.1002/aoc.7344
151. N. Ahmad, S. Rasheed, M.I. Nabeel, W. Ahmad, A. Mohyuddin, S.G. Musharraf, M. Najam-ul-Haq, D. Hussain, Stearic Acid and CeO2 Nanoparticles Co-Functionalized Cotton Fabric with Enhanced UV-Block, Self-Cleaning, Water-Repellent, and Antibacterial Properties, Langmuir 39(33) (2023) 11571-11581. https://doi.org/10.1021/ac 002.
152. Yichen Bai, Wei Mao, Yuqing Wu, Yunhang Gao, and Tianye Wang, "Synthesis of Novel Ternary Heterojunctions via Bi2WO6 coupling with CuS and g-C3N4 for the Highly Efficient Visible-light Photodegradation of Ciprofloxacin in Wastewater," Sep. 2020. https://doi.org/10.1016/j.colsurfa.2020.125481
153. Arif, S., Rasheed, S., Nabeel, M. I., Ahmad, W., Riaz, M. T., Musharraf, S. G., & Hussain, D. (2025). Enhanced Photocatalytic Activity of Sulfur–Nitrogen Co-Doped TiO2 Nanoparticles Synthesized using Dactylorhiza hatagirea Root Extract. ChemistrySelect, 10(34), e01568 https://doi.org/10.1002/slct.202501568.
154. G. Palanisamy, Nora Hamad Al-Shaalan, K. Bhuvaneswari, G. Bharathi, and G. Bharath, "An efficient and magnetically recoverable g-C3N4/ZnS/CoFe2O4 nanocomposite for sustainable photodegradation of organic dye under UV–visible light illumination," Jun. 2021. https://doi.org/10.1016/j.envres.2021.111429
155. Joseph, C.G., Anisuzzaman, S.M., Masjidin, N.N.D., Masjidin, D., Moktar, A.S., Nasir, W., M. I. Nabeel, Tahir, N. and Bade, A., 2026. Removal of residual antibiotics from aquaculture wastewater using ozonation and sonochemical treatment processes: a comprehensive review. Chemical Papers, pp.1-34. (2026), http://doi.org/10.1007/s11696-026-04687-8.
156. N. Ahmad, T. Ali, T.,. Nabeel, K. Ahmed, H. Baggash, M. Hasnain, & D. Hussain, (2025). Facile modification of nylon filter via vacuum coating with chitosan@ MCM-41/GO for efficient oily wastewater treatment. Journal of Materials Chemistry A. https://doi.org/10.1039/D5TA02462E.
157. Affandi, N. A., Joseph, C. G., M. I. Nabeel, Abd Majid, M. H., & Ghazali, K. Photolytic and Photocatalytic Degradation of Detergent and Surfactant Solutions by Various Light Sources Malaysian Journal of Chemistry, (2025), Vol. 27(6), 41-63 https://doi.org/10.55373/mjchem.v27i6.41.
158. Akshay Verma, Pooja Dhiman, Chin Wei Lai, Mu. Naushad, and Alberto García-Peñas, "Fabrication of visible light-driven magnetically separable Ag3PO4/Fe3O4/g-C3N4 photo catalyst for tetracycline degradation," Jul. 2025. https://doi.org/10.1007/s11051-025-06392-1
159. Jiajia Wang, Lin Tang, Guangming Zeng, Yani Liu, and Yaoyu Zhou, "Plasmonic Bi Metal Deposition and g-C3N4 coating on Bi2WO6 Microspheres for Efficient Visible Light Photocatalysis," Nov. 2016. https://doi.org/10.1021/acssuschemeng.6b02351